Developing a Pulsar Search Algorithm

Prepared by:

Roger Deane

Prepared for:

Department of Electrical Engineering

University of Cape Town

Supervisor: Professor Mike Inggs

October 2006

Declaration

I declare that this project report is my own, unaided work. It is a project report submitted to the Department of Electrical Engineering, University of Cape Town, in partial fulfilment of the requirements for the degree of Bachelor of Science in Engineering. It has not been submitted before for any degree or examination at any other university.

. . . .

Roger Deane

Cape Town

23rd October 2006

Acknowledgements

I would like to thank Tsepo Montsi for his immense help with programming in C code and using a Linux based operating system. His commitment persevered despite fasting for Raamadaan for an entire month during the project.

I would like to thank my supervisor, Prof Mike Inggs, for managing to give advice and direction despite currently being at the forefront of South Africa's biggest technology drive, the Karoo Array Telescope (KAT).

Dr Duncan Lorimer provided some very useful advice via email contact. An enormous amount of thanks to him for helping a student he had never met on the other side of the planet.

I would like to thank George Eadie for proof-reading this thesis with great scrutiny at such late notice.

Finally, I would like to thank my mother whose strength in trying circumstances will forever serve as a great source of inspiration.

Abstract

Pulsar searching is a highly intensive computational process involving enormous data sets and iterations through unknown parameters. This thesis aims at developing a simple algorithm capable of recovering the pulsar signal from below the receiver noise level. The relevant theory required to achieve this is researched. The algorithm has been coded in C to gain a speed advantage over scripting languages. It accounts for interstellar dispersion and performs an array of procedures to increase probability of detecting the pulsar signal.

Table of Contents

List of Figures

List of Tables

Chapter 1

Introduction

1.1 Project Background

Pulsars are rapidly rotating, highly magnetic neutron stars that emit a sweeping, lighthouse-like beam of radiation. They have a number of unique characteristics and properties that enable them to be used as 'cosmic laboratories' to test physical laws in extreme environments. The reason for this is that the pulsar environment cannot be reproduced on Earth. They also have remarkably accurate spin periods that make them the most accurate clocks in the Universe. Particle physics, General and Special Relativity as well monitoring Earth's seismic activity are just a few of the the fields that use pulsars as tools to perform experiments.

The pulsar population is currently limited to approximately 2000. An increase in the population will not only lead to larger sample space to perform a multitude of scientific experiments, but also to the discovery of exotic systems that are closer the limits of physics than previously observed.

The search and discovery of pulsars clearly forges a path forward for an array of scientific disciplines.

1.2 Project Objectives

The primary aim of this project was to gain a theoretical background to the physical attributes of pulsars that are important in their detection and with this knowledge produce a relatively general C code algorithm. 'General' meaning that the code can be tailored to the specific parameters of the radio telescope used, as well as the type of search that is desired. A secondary objective was to make the algorithm as computationally efficient as possible, however,simplicity and complete understanding were prioritised above speed.

1.3 Problem Statement

Pulsar searching is conceptually a simple process of detecting a periodic signal in a given parameter space. It is complicated by unknown search parameters and the need to model physical characteristics and processes of the Galaxy and the pulsars themselves. The periodic signal tends to be buried below the receiver noise level due to its low amplitude as well as a smearing of signal as it travels through the interstellar medium (ISM). The unknown parameters lead to the use of iterations through trial values. This results in large processing requirements. Further complications arise with the fact that the system parameters of the radio telescope array to be used, determine the effectiveness of the search procedure adopted. Thus, during the development of the Pulsar Search Algorithm a range of concepts must be assessed in order to determine the optimal relationship between hardware, software and astrophysical object as to maximise the performance of the algorithm. In essence, one is trying to find a trade-off between sensitivity and computational time.

1.4 Scope and Limitations of Investigation

The scope of this project is to produce a working framework of a generic pulsar search algorithm. Future additions and extensions can be made for specific searches involving

binary systems, Galactic core searches and perhaps even extragalactic searches depending on the radio telescope used.

The project required that two new skills be learnt: using a Linux based operating system and programming in C code. This was time consuming and limited the number of extensions made to the generic pulsar search algorithm.

1.5 Document Outline

Chapter 2 shows that the pulsar signal path can be split into three parts: originating at the source; traversing the ISM; and finally arriving at the telescope receiver and being analysed by the post-processing software. The chapter starts by providing a theoretical background on the pulsar structure, radiation mechanisms and processes with particular reference to the characteristics of the radio radiation produced. The effects of the ISM on pulsar signal are described so as to gain an understanding on how these can be compensated for. Generic methods for detecting pulsars are explained as well as their advantages and disadvantages compared. The chapter closes with a description of barycentering and its importance.

Chapter 3 describes the implementation of the algorithm in the form of C code. It was decided to use the more computationally efficient frequency domain method. A channelized, time series input data file with header information is loaded for processing. The file header provides the algorithm with all global variables needed. Detail on how the algorithm accounts for dispersion in the time domain is given. The resulting time series is transformed into the frequency domain. Due to the volume of radio telescope data, this is computationally expensive process and so various methods of making this more efficient are explained. With data now de-dispersed and transformed into the frequency domain, the spectrum can be searched for significant amplitudes. However, a number of techniques can be implemented to increase the signal to noise ratio and hence sensitivity to the pulsar signal. These techniques are discussed in the required detail. A threshold detection test is then carried out and the selection of this threshold level is commented on.

The relevant parameters of pulsar candidates found are stored for re-evaluation by a pulsar astronomer.

Chapter 4 reports the algorithm's performance in the processing of simulated pulsar data. The data is obtained from a package called SIGPROC written by Dr Duncan Lorimer, a pulsar astronomer. A number of different parameters can be simulated. The approach in testing is to simulate a typical pulsar and monitor the path of the data through the various stages of the algorithm. In this way the workings of each function are illustrated and quantified.

Chapter 5 lists the conclusions made from the results and determines if the project's objectives have been satisfied. Possible additions and extensions to the algorithm are also discussed.

Chapter 2

Literature Review

This chapter shows that the pulsar signal path can be split into three parts: originating at the source; traversing the ISM; and finally arriving at the telescope receiver and being analysed by the post-processing software. The chapter starts by providing a theoretical background on the pulsar structure, radiation mechanisms and processes with particular reference to the characteristics of the radio radiation produced. The effects of the ISM on pulsar signal are described so as to gain an understanding on how these can be compensated for. Generic methods for detecting pulsars are explained as well as their advantages and disadvantages compared. The chapter closes with an overview of previously conducted searches and their strategies.

2.1 The Physics of Pulsars

Pulsar Astronomy is a relatively young field as the first pulsar was only discovered in 1967 and although an enormous amount of work has been done and progress made, there are still disagreements on the basic structure and emission mechanisms of pulsars. Thus, a fairly simplistic model of the pulsar will be described that is sufficient for understanding the methods required to detect them.

2.1.1 Structure

A pulsar is a rapidly rotating neutron star, emitting two beams of EM radiation with a period equal to the rotation period. A neutron star is a highly dense remnant of type II b supernovae. Its density is approximately half that of a neutron. A typical pulsar has a radius of 10 km, mass of 1.4 solar masses (1 solar mass = 1.99 x10^{30} kg), magnetic field intensity of 10^{12} Gauss and a period ranging between 1.6 milliseconds and 8.5 seconds. The rapid spin rate is attributed to dramatic decrease in radius by several orders of magnitude during the supernova rapid contraction stage. The law of conservation of angular momentum requires that a rotating body's rotational velocity must increase if the radius decreases. The strong magnetic field intensity is attributed to the decrease in area through which the flux permeates as well as the increase in the spin period and hence magnetic field generated by the rotating core dynamo effect.

Models for the equation of state at the pulsar's highly dense states of matter are uncertain as equivalent conditions cannot be reproduced in terrestrial laboratories. The size of a star is determined by the opposing forces of gravity and pressure. The equation of hydrostatic equilibrium governs this:

$$\frac{dP}{dr} = \frac{(G.m(r)\rho)}{r^2} \qquad \text{(Eq. 2.1)}$$

where: P   =   pressure
         G   =   gravitational constant
         r   =   radius
         m(r) =   mass of the star as a function of its radius
         ρ   =   density

This however quickly becomes complicated at extreme densities due to the force of gravity becoming comparable to the electrostatic forces between the fundamental particles of matter. It is at these high energies that electrostatic forces between electrons and protons are overcome. The two particles fuse to form neutrons. Depending on the pressure,

different states of these neutrons are prevalent. Figure 2.1 gives a cross-section of neutron star showing the predicted structure for a 16 km radius model:

Figure 2.1: Diagram showing a theoretical model of internal structure of a neutron star and its different states of matter. [12]
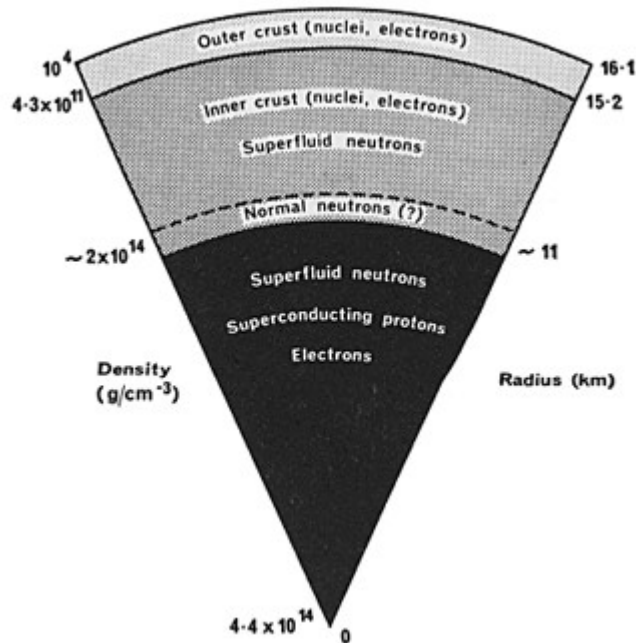
Standard models of a 1.4 solar mass neutron star predict a diameter of 10 km. It is interesting to note that neutron stars are on the very edge of becoming black holes. The Schwarzchild radius defines the perimeter around a black hole within in which light cannot escape the gravitational pull of the black hole. A 1.4 solar mass neutron star with a radius of 10 km has just two and a half times the radius of a black hole of the same mass.

2.1.2 Magnetic Field and Pulsar Atmosphere

Pulsars have enormous magnetic field strengths due to the magnetic flux of the infalling star being conserved in a vastly smaller area. Typical values are $10^{11\text{-}12}$ Gauss at the poles [3]. A misaligned magnetic and rotational axis results in a changing magnetic field thus inducing an electric field via Maxwell's equation:

$$\frac{\partial \Psi_M}{\partial t} = -\oint \vec{E} \cdot dl \qquad \text{(Eq. 2.2)}$$

The induced electric field is sufficiently strong (by several orders of magnitudes) to overcome the gravitational force on the surface around the magnetic poles. This results in particles being ripped from the surface of the neutron star and, being magnetically locked, co-rotating with the star. [1]

The magnetic field dominates all physical processes in the pulsar atmosphere. The only effect the magnetic field has on the internal structure is on the crystalline neutron crust. [2]

The magnetic field and rotation of the pulsar form what is termed the magnetosphere. These particles become part of a 'sea' of high energy plasma. These particles travel along magnetic field lines from the pole to pole. Solid body rotation occurs in the magnetosphere due to the high energy plasma being magnetically locked to the field lines. Thus there exists a radius from the pulsar at which a particle must travel at the speed of light in order to continue co-rotating with the pulsar. This radius defines the boundary of the light cylinder, centred on the rotation axis. It can easily be calculated given the angular velocity or period:

$$R_c = \frac{c}{\omega} \qquad \text{(Eq. 2.3)}$$

where: c = speed of light
           ω = angular velocity

Figure 2.2   Illustration of the concept of a light cylinder. It is defined as the radius at which matter in the magnetosphere must travel at the speed of light to continue co-rotating with the neutron star. Credit: [8].
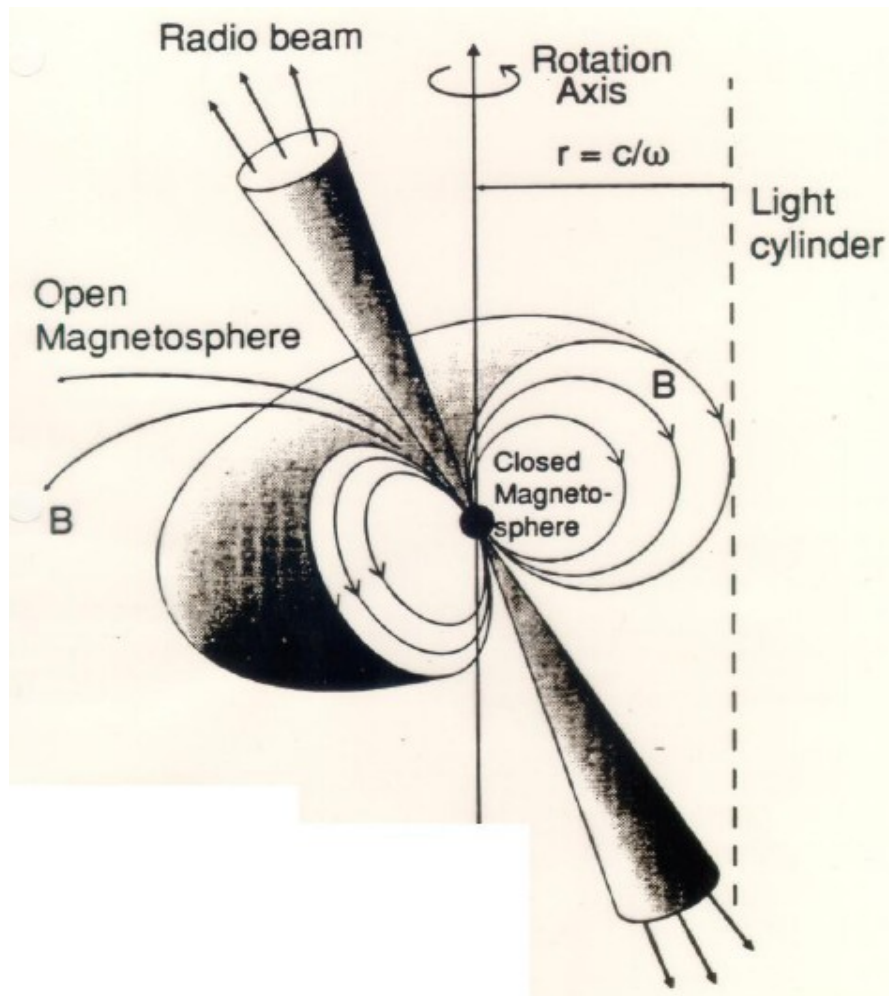
As stated previously, particles are confined to moving along magnetic field lines. Particles travelling along a closed field line (i.e. A field line that does not traverse the light cylinder) will return to the surface of the pulsar at the opposite pole. Particles travelling along an open field line will approximate the speed of light as they approach R_c. As this occurs the particles escape from the magnetosphere. Radiation is confined to the region on the pulsar pole that contains open magnetic field lines as this is where particles obtain relativistic velocities. This is referred to as the polar cap region [2].

2.1.3 Pulse Attributes

As discussed, pulsar radiation is emitted from a confined region above the pulsar called the polar cap. This coupled with the misaligned magnetic and rotation axes causes the rapidly spinning neutron star to behave in a lighthouse fashion. If the earth is in the radiation path, a periodic pulse is observed. This is illustrated in Figure 2.2.

Figure 2.3: Illustration of pulsar beam: a) intersecting Earth's orbital position in which case a pulse can be detected; b) not intersecting Earth's orbital position yielding the pulsar undetectable. Credit: [14]
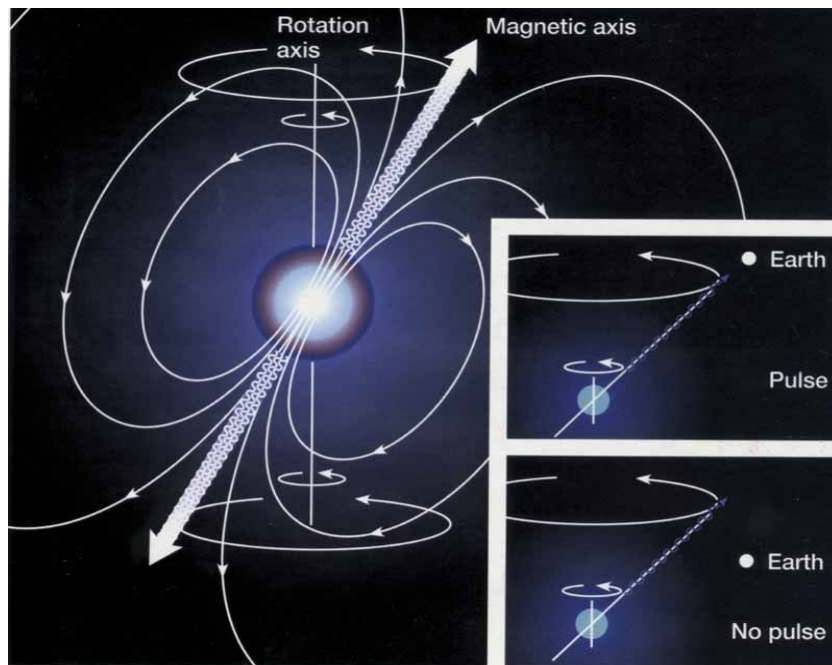
Before discussing the pulses in any detail, the typical flux density level emission frequency ranges will be given as a general idea in the descriptions that follow. The unit of flux density measured by a radio telescope is the Jansky, named after Karl Jansky who accidentally discovered extraterrestrial radio frequency (RF) radiation in 1931 while working as a radio engineer at the Bell Telephone Laboratories in Holmdel, New Jersey.

1 Jansky (Jy) = 10^{-26} W.m^{-2}.Hz^{-1}. In 2005 the public domain catalogue, [10], contained flux densities for 908 pulsars measured at 1.4 GHz. The range was between 20µJy and 5 Jy,

with a median of 0.8 mJy [1]. These figures indicate the extremely weak nature of the pulsar signal.

2.1.3.1 Pulse Components

It is interesting to note that every pulse is different. However, once a sample of approximately one hundred or more pulses have been integrated together the pulse profile stays remarkably constant [2].

Individual pulses, however, vary on many different levels. The pulse will ordinarily have a major component and a number of other minor components, all of which are Gaussian in form. 3 ± 1 components are seen for normal pulsars. If sufficient signal to noise (S/N) and time resolution is available then what is known as microstructure can be observed [1]. If the time series data can be resolved down to nanosecond level, the so-called giant pulses can potentially be observed. The Crab nebula is known to emit giant pulses of flux density three orders of magnitude higher than the mean pulse level [1]. This phenomenon enables the possibility of discovering a pulsar directly from a giant pulse.

2.1.3.2 Duty Cycle

Significant use of the terms *duty cycle* and *pulse width* are used in this document. The former is used in Communications Engineering documents because generally a signal is either termed a binary 0 or 1. In scientific documents, the term pulse width is used and is defined as the area underneath a pulse divided by its peak height. Although, pulse profiles are made up of Gaussian components as outlined in section 2.1.3.1, they are modelled as rectangular pulses for conceptual ease. Thus, the document refers to the duty cycle which is an equivalent to pulse width.

Pulsar duty cycles range between 1% and 50% with typical values of 5% [1]. The effect of this duty cycle is discussed later in the report.

2.1.3.3 Interpulses

Some pulsars are known to emit interpulses. These lower amplitude pulses occurring between main pulses can be explained by radiation from the opposite pole of the main pulse radiation [1].

2.1.3.4 Pulse Profile Frequency Dependence

The pulse profile shape is dependent on observing frequency . The radius-to-frequency mapping states that the increase in pulse width when observed at lower frequencies can be attributed to higher frequencies of radiation being generated closer to the pulsar surface and therefore confined to a smaller area than their lower frequency counterparts [2]. This trend is not as prevalent in millisecond pulsar profiles. Although not found in any of the sources researched it is assumed that this due to the Huygens angle: $\varphi = \lambda / D$, where φ is the far field angle and λ is the radiation wavelength. D is aperture of the radiation area.

2.1.3.5 Polarization

Pulsar radiation is amongst the most polarized sources of radiation in the Universe. This is due the extreme magnetic fields present at the source of the radiation. It is further polarized by non-spherical dust grains in the ISM that are aligned by the Galactic magnetic field. Thus, the radio telescope should use two orthogonal orientations of waveguides. The algorithm assumes that the two electric field vectors have been suitably combined by front end hardware/software.

2.1.4 Radio Emission Processes

Now that a general idea of the type of signals received at the radio telescope have been discussed, the origin of this radiation must be described. During the process of material being ripped from the surface and being released from the neutron star's influence, various electromagnetic emission processes take place. This is perhaps the most poorly understood area in the study of the pulsar. Astronomer Jon Arons has said that we know why pulsars pulse, but not how they shine. This does not greatly impact the search technique as the type of radiation received is known. It occurs in a broad range of the spectrum from the radio right through to gamma rays, however, the radiation is usually strongest in the radio division of the spectrum in the region of 100 MHz to 100 GHz.

2.1.4.1 Synchrotron Radiation

Synchrotron radiation occurs when electrons spiral along a magnetic field line. From the equation:

$$\vec{F}_m = \frac{q}{c} \, \vec{v} \times \vec{B} \qquad\qquad (Eq. \ 2.4)$$

it can be seen that the electron experiences an acceleration vector towards the centre of the spiral to change the direction of the velocity vector $\vec{v}$. From fundamentals it is known that radiation is caused by acceleration of charge. This type of radiation is usually strongly polarized in the plane of particle rotation around the magnetic field line.

2.1.4.2 Curvature Radiation

Curvature radiation occurs when a particle travelling along a curved magnetic field line. It thus experiences an acceleration of the same form given by equation 2.4 and thus must emit radiation. This radiation is usually strongly polarized in the plane of the curved magnetic field line.

2.1.4.3 Antenna Radiating Mechanism

Antenna mechanism models assume N particles of charge q occupy a volume smaller than half the emitted wavelength. This allows the the N particles to all radiate in phase, and hence behaving as a particle of charge Nq. The emitted power is then increased by a factor N^2 as opposed to N in the incoherent radiating case. This is thought to occur above the polar cap [2].

2.2   The Interstellar Medium

This section discusses the plasma that makes up the interstellar medium (ISM) and the physics involved that determines the effects it has on EM waves passing through it.

2.2.1 Composition and Distribution

The ISM is comprised of ionized plasma at typical temperatures between $30 - 80$ K. This medium has a refractive index that differs appreciably from unity and hence affects the path of any EM wave propagating through it. The refraction experienced is frequency dependent and is given by:

$$\mu \;=\; \left(1 - \left(\frac{f_p}{f} \right)^2 \right)^{\frac{1}{2}} \qquad\qquad \text{(Eq. 2.5)}$$

where: f is the observing frequency

f_p is the plasma frequency

A wave will not propagate if the plasma frequency is greater than the observing frequency.

The plasma frequency is given by:

$$f_p = \left(\frac{c^2 n_e}{\pi m_e}\right)^{\frac{1}{2}} = 8.5\,\text{kHz}\left(\frac{n_e}{\text{cm}^{-3}}\right)^{\frac{1}{2}} \qquad \text{(Eq. 2.6)}$$

where: c = speed of light = 299 792 km/s

n_e = electron number density

m_e = mass of an electron = 9.11 x 10^{-31} kg

Typical values for electron density in the ISM according to [7] are 0.03 cm^{-3}. This value gives a plasma frequency (f_p) of approximately 1.5 kHz. However, electron density is highly dependent on galactic co-ordinates. The Milky Way is a spiral galaxy with a higher concentration of plasma in the galactic plane than in the halo. The sun is positioned 8.5 kiloparsec (1 parsec = 3.086 x 10^{16} metres) from the galactic centre in the galactic plane. The expected electron density will naturally be dependent on the line of sight of the pulsar from Earth. More detail on this will be discussed later in the text.

Some of the effects the ISM has on a propagating EM wave include:

- Dispersion
- Scintillation
- Scattering

A brief overview of each of these follows.

2.2.2 Interstellar Medium Effects

2.2.2.1 Dispersion

Dispersion has the effect of introducing a time delay on the propagating EM wave. However, this time delay is dependent on observing frequency and electron content in the propagation path, therefore the pulse is spread or dispersed in the time domain.

The group velocity of a travelling wave is given by:

$$v_g = c\,\mu \qquad \text{(Eq. 2.7)}$$

where the refractive index (μ) of the ISM is less than unity.

Thus the delay experienced by a radio signal travelling between the pulsar and Earth with respect to the speed of light is:

$$t = {}_0\!\int^d \frac{1}{v_g}.dl - \frac{d}{c} \qquad \text{(Eq. 2.8)}$$

Making the appropriate substitutions seen in Appendix A1 leads the following expression for the time delay:

$$t = \frac{D_{const} \times DM}{f_2} \qquad \text{(Eq 2.9)}$$

where:

$$DM = {}_0\!\int^d n_e.dl \qquad \text{(Eq. 2.10)}$$

This is referred to as the dispersion measure. It is expressed in $cm^{-3}pc$.

D_{const} is referred to as the dispersion constant given by:

$$D_{const} = \frac{e^2}{2\pi \cdot m_e c} = (4.148808 \pm 0.000003) \times 10^3 \, \text{MHz}^2 \, \text{pc}^{-1} \, \text{cm}^3 \, \text{s} \quad \text{(Eq. 2.11)}$$

The uncertainty here is due to the current uncertainty in the mass and charge of an electron (m_e and e respectively).

The time delay between two frequencies can now be represented by the expression:

$$\Delta t \approx 4.15 \times 10^6 \, \text{ms} \times \left(f_1^{-2} - f_2^{-2} \right) \times DM \quad \text{(Eq. 2.12)}$$

Note that the figure $(4.148808 \pm 0.000003) \times 10^3$ MHz^2 pc^{-1} cm^3 s has been rounded off to 4.15×10^6 ms, however in all calculations the full accuracy will be used. Clearly the DM can be inferred by measuring the pulse delay between two observed frequencies. Hence, electron content of the propagation path can be determined if the distance is known or vice versa.

17

Figure 2.4: Dispersed pulses from the Vela pulsar. The bottom trace shows the profile obtained by de-dispersing and summing the other traces. The asymmetric nature of the pulse profile is due to interstellar scattering.

18
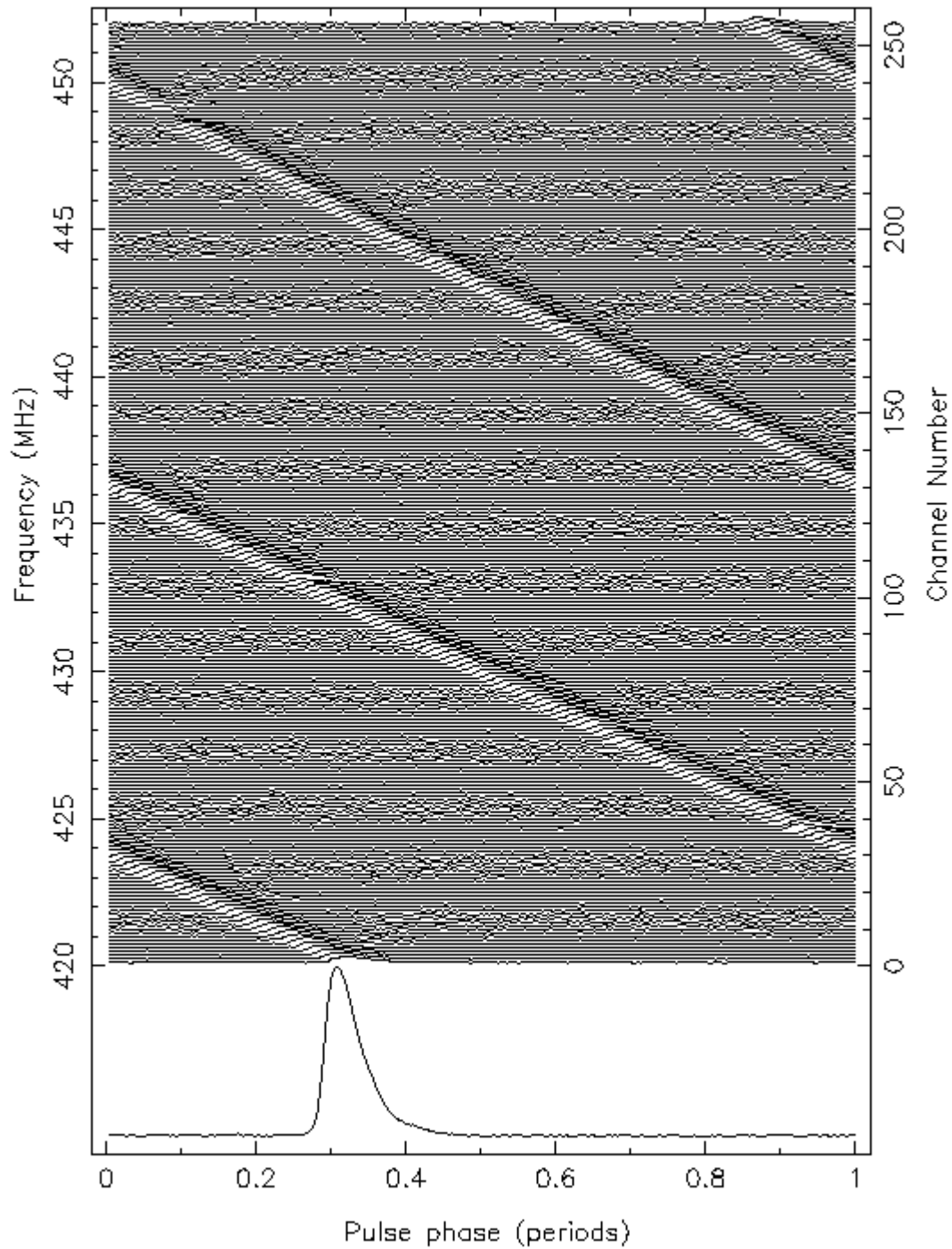
2.2.2.2 Scintillation

Scintillation is the equivalent of fading in Radio Frequency and Microwave engineering i.e. It is a fluctuation in power level of the signal over relatively short time periods. The ISM has an irregular structure at a number of different scales with clumps and voids of matter. In addition to this, it is largely turbulent due to the differential rotation of the Galaxy and strong sources of radiation. These two effects cause multipath propagation of the radio signal as they refract through electron clouds. Multipath propagation results in a spread in arrival time of a respective frequency. This can cause a large degree of interference depending on the difference in path lengths [2].

Large scale turbulence causes a slower variation in intensity on the time-scale of years, whereas smaller scale turbulence causes turbulence over a time-scale of minutes [2].

2.2.2.3 Scattering

Scattering occurs as an EM wave interacts with electron content in the ISM. It causes the direction of the EM wave to be changed, decreasing the intensity of the radiation in the original direction of propagation. Lower frequencies tend to be scattered more efficiently, causing a smearing of the pulse and hence an asymmetry in the received pulse profile due to the lower intensities of the low frequencies [2]. Scattering due to interstellar gas is relatively insignificant compared to the dispersion effects [16]. Figure 2.5 illustrates the the two effects discribed.

Figure 2.5: Scattering of the Vela pulsar showing the asymmetry
introduced by scattering at lower observing frequencies. Credit: [2]
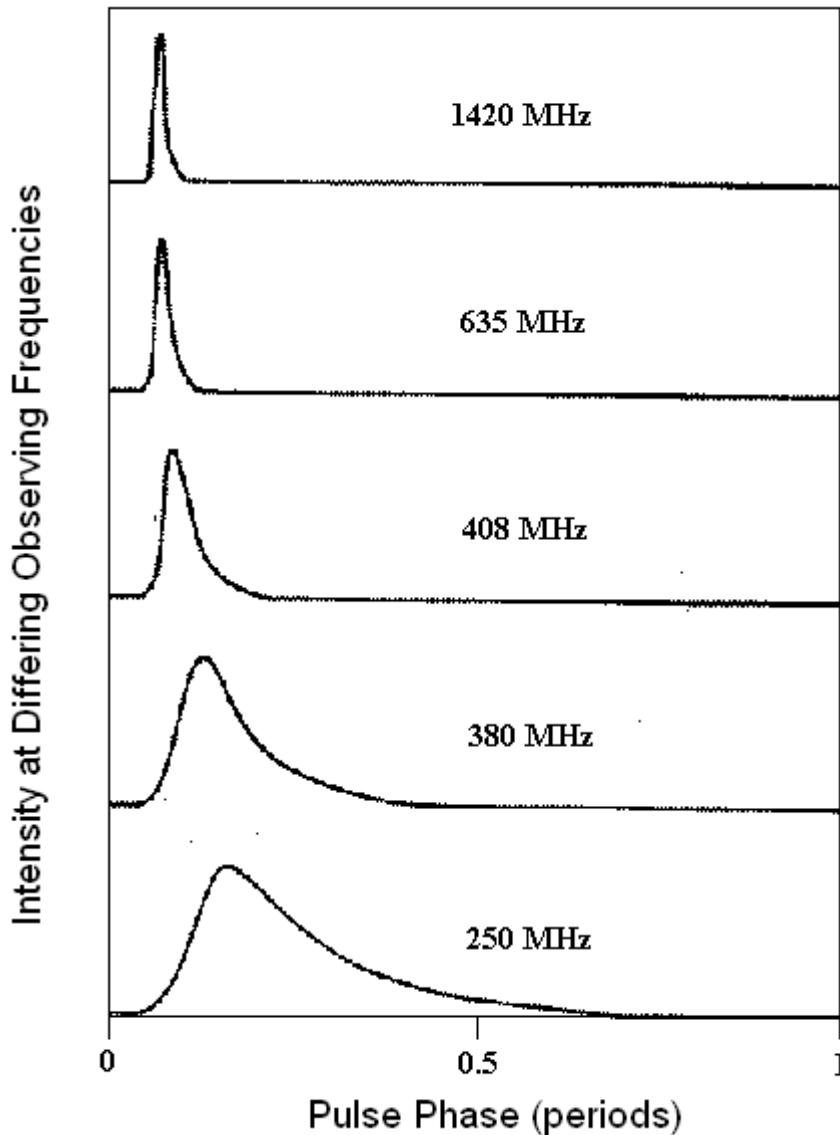
2.2.3 Galactic Electron Density Model

The Milky Way is a spiral galaxy and thus has matter concentrated in the plane of the spiral arms, with an increasing density towards the core and within the spiral arms. The Dispersion Measure to be expected is thus dependent on the position of the line of sight of the telescope. Two papers written by Cordes and Lazio [12],[13] provide a very detailed model of electron density in the Galaxy and how to implement the model. The concept used in pulsar searches is that there is a maximum expected DM due to the interstellar

medium of our galaxy at each line of sight of the telescope. These maximum expected values are derived from previously discovered pulsars as well as angular broadening measurements on non-pulsar Galactic sources and extragalactic sources. The Equatorial co-ordinates of the telescope beam are transformed to Galactic co-ordinates to enable an easier series of conditional statements to determine the maximum trial DM value.

2.3 Different Search Techniques

The periodic signal of a pulsar is hidden in the random noise of the output data stream of the radio telescope receiver. An arbitrary region of sky could contain a pulsar signal of unknown period or pulse length. There are a number of methods of extracting the periodic signal from the raw data. Two main techniques are introduced here. The first uses time domain analysis by searching for the train of pulses directly once de-dispersion has been performed. This is also called periodogram analysis in some texts. The second method involves taking the Fourier transform of the time series and examining its spectrum for any large amplitude contributions. This method is used in most modern searches as it is far more computationally efficient.

2.3.1 Periodogram Analysis

A time series of length N is folded modulo a trial pulsar period value and the resulting pulse profile is examined for any statistically significant features. A window function of varying length is used to search the resulting data series for possible pulse profiles. This windowing must be performed at a range of different widths as the expected duty cycle can range from 1% to 50%. The range of trial period values would have a possible range of 1 millisecond to 10 seconds considering the shortest period pulsar is 1.6 ms while the longest period is 8.5 s. This requires enormous computational power considering the accuracy of trial period required to obtain a significant pulse profile. A weak signal will not be detected unless the trial period is sufficiently close to the intrinsic pulsar period. Another consideration is the large data lengths obtained from modern searches due to higher sampling rates. This lengthens time domain analyses considerably. Nonetheless, there

certainly is scope for this search technique, particularly if the trial period range can be considerably narrowed and if the range of values are relatively long (P > 2 s) [2]. Long periods require lower sampling data rates and hence shorter computational time. Another advantage is that these objects are shown in a substantially small part of the Fourier Spectrum and it is at low frequencies that the effect of red noise is most prevalent. These two factors allow longer period pulsars to be detected with greater ease and accuracy using the Periodogram Analysis method [2].

Time domain search speeds were significantly increased by the introduction of the Fast Folding Algorithm (FFA) [2]. Here, a time series of length N_{tot} is split into N_{seg} contiguous segments such that N_{tot}/N_{seg} is an integer power of 2. The time series is then folded modulo over a range of values for N_{seg}, and hence period as Period = $N_{seg}.t_{samp}$.
A derivation shows that normal folding requires $N_{tot}[(N_{tot}/N_{seg}) - 1]$ additions, while the FFA only requires $N_{tot}.\log_2(N_{tot}/N_{seg})$, saving a great deal of computational power for long time series [1].

2.3.2 Frequency Domain Methods

The more popular, modern method is to compute the Fourier Transform of the de-dispersed time series and search for any significant spectrum features. This transformed time series will contain a large amplitude at the fundamental pulsar frequency as well as a number of harmonics comparable in amplitude to the fundamental. The number of harmonics is usually estimated by the reciprocal of the duty cycle. Thus, a method to increase the S/N ratio, is to retrieve the power in these harmonics in some way.

Because the pulsar data is a discrete set of time samples, the Discrete Fourier Transform (DFT) must be implemented. The DFT has the property that it converts a real time series to a set of Fourier components that are symmetric about the Nyquist frequency (half the sampling frequency). This redundancy can be used to half the computation time. Further speed advantages can be taken by using multi radix Fast Fourier Transform (FFT) where the total number of samples is a multiple of prime factors. The number of multiplications and additions can be significantly reduced, particularly for large values N which is usually the case for radio telescope data.

2.4 Barycentering

Barycentering involves adjusting the pulse arrival time at the radio telescope to that of the Solar System Barycentre (SSB) which provides a sufficiently accurate Local Standard of Rest. This is done because during any extended integration time the Earth revolves a significant distance in its orbit around the SSB causing a de-linearisation of the periodic pulse and hence a smearing of the frequency amplitude in the frequency domain and loss in signal to noise ratio. It has been suggested that this should be performed for any integrations that last longer than 30 minutes [1]. The full expression for barycentric corrections includes factors such as the Einstein delay and the Shapiro delay which correct for the slowing of clock time in the presence of the SSB gravitational well; and the increase in photon distance to the SSB due to photon bending around the major bodies in the Solar System respectively. This type of resolution is clearly only needed in pulsar timing applications. The major contributor that will increase S/N for long integrations is the geometric correction. This compensates for the difference in pulse arrival between Earth and the SSB due to their positions relative to the observed pulsar. The delay is given by equation 2.12:

$$\text{time correction} \; = \; \left(\vec{r}_{obs} \; \cdot \; \hat{n} \right)/c$$

(Eq. 2.13)

where: $\vec{r}_{obs}$ is the vector from SSB to the observatory

$\hat{n}$ is a unit vector from the observatory in the direction of the pulsar

c is the speed of light

A simple diagram illustrates the process in Figure 2.6.

Figure 2.6: Diagram illustrating the need for barycentering for long integrations. The Earth's velocity relative to the pulsar changes during an observation, de-linearising the period and hence decreasing the S/N ratio in the frequency domain. The pulse arrival times must therefore be referenced to a Local Standard of Rest. The Solar System Barycentre is a sufficient approximation.
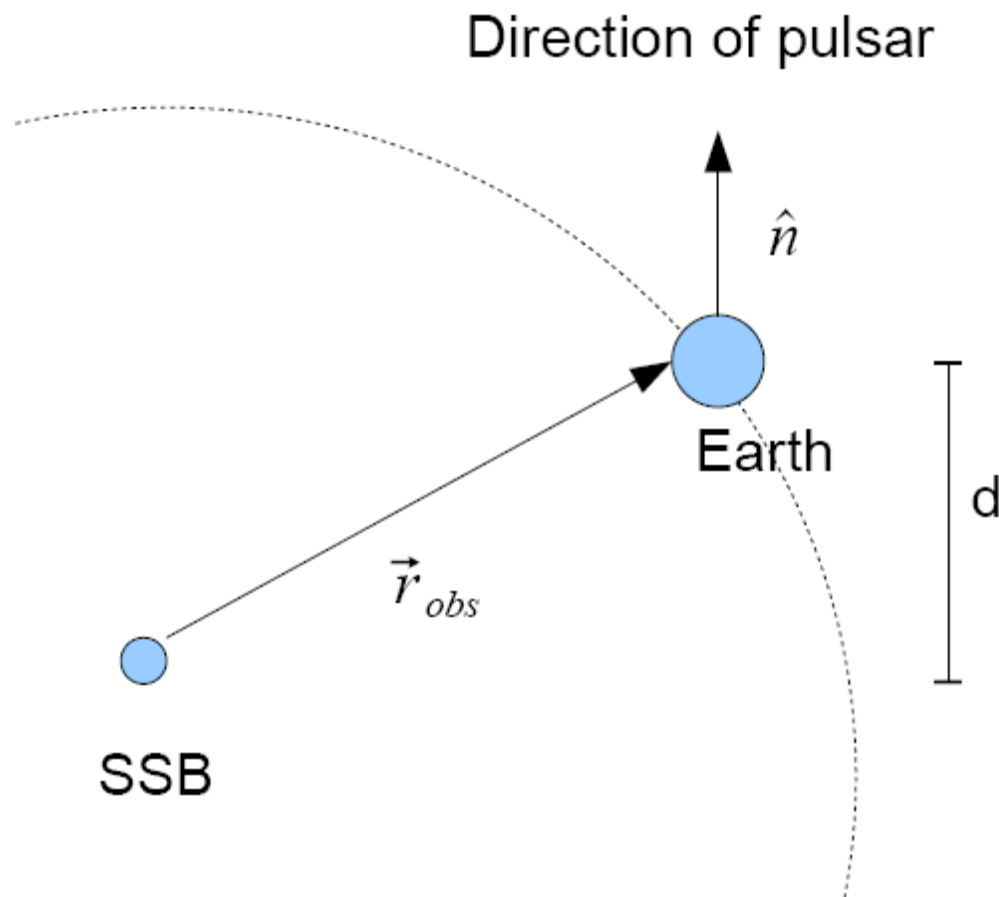
As Earth orbits the SSB (along dotted line), the distance differential, d, between them changes. The distance between the Earth and the SSB is far smaller than the distance of any potential pulsar to Earth, thus the radiation can be assumed to be a plane wave with wavefront perpendicular to $\hat{n}$. The time difference can be compensated for by equation 2.13, however the two vector quantities require an array of coefficients published by NASA's Jet Propulsion Laboratory.

Chapter 3

Implementation

This chapter describes the implementation of the algorithm in the form of C code. It was decided to use the more computationally efficient frequency domain method. A channelized, time series input data file is loaded for processing. The file contains a header that provides the algorithm with all global variables needed. Details on how the algorithm accounts for dispersion in the time domain is given. The resulting time series is transformed into the frequency domain. Due to the volume of radio telescope data, this is computationally expensive process and so various methods of making this more efficient are explained. With data now de-dispersed and transformed into the frequency domain, the spectrum can be searched for significant amplitudes. However, a number of techniques can be implemented to increase the signal to noise ratio and hence sensitivity to the pulsar signal. These techniques are discussed in the required detail for the reader. A threshold detection test is then carried out and the selection of this threshold level is commented on. The relevant parameters of pulsar candidates found are written to a file for re-evaluation by an astronomer.

3.1 Programming Language

The algorithm was written in the C programming language to gain as much of a speed advantage as possible. The overhead required for operations using a scripting language is considerably larger. The DFT library was downloaded from www.fftw.org. The Fourier Transform code optimises itself to the hardware running it by automatically inputting the system parameters and tailoring the transform computations based on that hardware.

3.2 Algorithm Overview

The algorithm implemented is based on the standard search procedure outlined by Lorimer and Kramer in [1] . Some of the operating parameters of the Karoo Array Telescope (KAT) have been used in the implementation, however a very general approach has been taken in the coding procedure, allowing the code to be modified with relative ease to fit the relevant hardware parameters. A list of the KAT operating parameters used is given in chapter 4 along with the simulations. Hardware parameters are stored as global variables thus enabling one change to change the respective value throughout the code. The algorithm's block diagram is shown in Figure 3.1.

Figure 3.1: Topological overview of the pulsar search algorithm. This the standard model outlined in [1]. It shows the input time series data being dispersed in the time domain and then transformed to the frequency domain to search for spectral features.
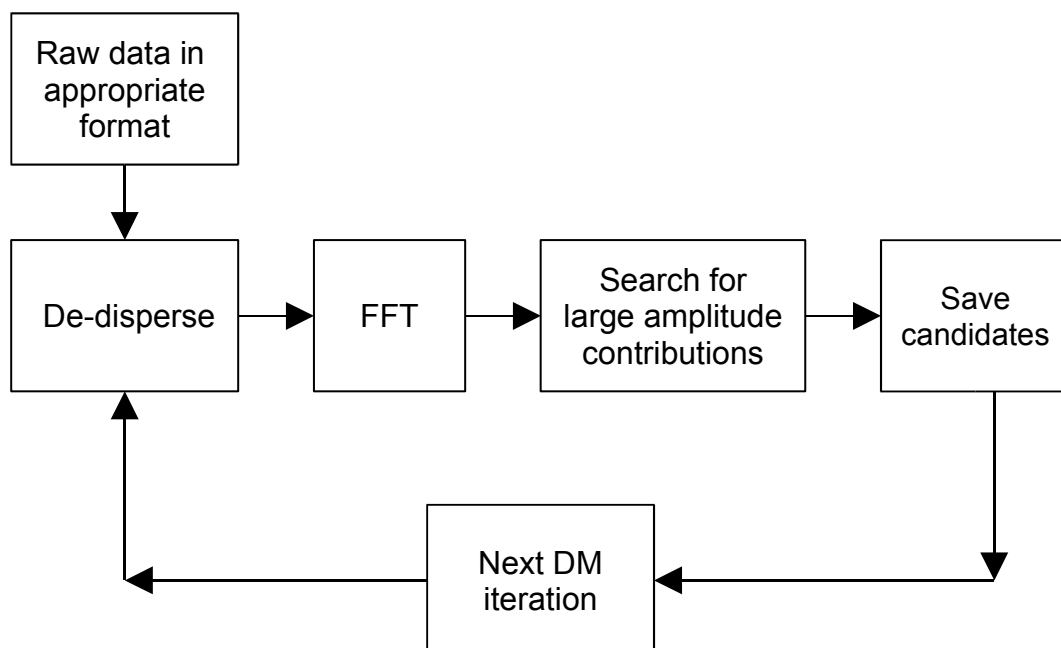
The respective blocks in the algorithm are now elaborated on.

3.3 Explanation of Main Functions

3.3.1 Simulated Data

Pulsar data was simulated using the SIGPROC package written primarily by Dr Duncan Lorimer. The package takes in a variety of pulsar parameters, however for purposes of this project only the following were used/varied:

- period
- duty cycle
- telescope beam co-ordinates
- dispersion measure
- observation time
- sampling time
- number of channels
- number of bits per time sample

The package outputs a file that contains a header with all input parameters as well as header and data size. The algorithm extracts all variables required for computational processes from the header. The data stream starts with the first time sample of highest frequency channel through to the lowest channel. Appended to that is the second time sample of the entire frequency channel range, and so on. The observation time, number of channels, sample time, and number of bits per sample are all known from the header file, thus enabling any time sample to easily be accessed by the use of indices. For example: if the ith sample of the jth channel has an index number = (i x number of channels) + j. Raw data is cast to the appropriate data type.

3.3.2 De-dispersion

Once the data has been read in and all global variables have been initialized, processing is ready to begin. The first function is de-dispersion. Recall equation 2.12 that expresses the relative time delay between two radiation frequencies traversing a region in space with a particular dispersion measure. This must now be related in terms of time samples. This involves division by the sample time giving an integer that is rounded off.

$$\text{time sample shift} \; = \; \frac{\Delta t}{t_{sample}} \; \approx \; \frac{4.15 \times 10^6 \; ms}{t_{sample}} \times \left(f_1^{-2} - f_2^{-2} \right) \times DM$$

(Eq. 3.1)

This calculation is performed for each channel and the appropriate binary shift carried out. An appropriately shifted channel time series is then added to an array referred to as sumChans in the code. This 'on-the-fly' addition avoids having to access the entire data set a second time to add up all the channels. For clarity, an example is given of dispersed time series before and after de-dispersion. The final de-dispersed time series that is the summation of all the channels is also shown. Note that the algorithm does not perform these steps separately, it is illustrated in this way purely for the purpose of visualization.

Figure 3.2: Matrix representation of a dispersed time series. The shaded blocks represent the position of the pulse in that particular frequency channel.

Frequency Channel [MHz]	Time Sample Number					
	0	1	2	3	4	...
1400	1	7	1	1	0	...
1350	0	1	7	1	0	...
1300	1	0	1	7	1	...
1250	1	0	1	1	7	...
...	...	...	...	...	...	...

Figure 3.2 shows a dispersed time series where pulse peaks at different frequencies have been delayed by different lengths of time. This results in a broadening of the pulse arrival time as well as a decrease in pulse amplitude.

Figure 3.3: Matrix representation of correctly de-dispersed time series data. The shaded blocks have now been positioned in the same time sample number, representing de-dispersion by the correct value of DM.

Frequency Channel [MHz]	Time Sample Number					
	0	**1**	**2**	**3**	**4**	**...**
1400	1	7	1	1	0	...
1350	1	7	0	1	0	...
1300	1	7	1	1	1	...
1250	1	7	1	0	1	...
...	...	...	...	...	...	...

Figure 3.3 shows the time series in Figure 3.2 that has been de-dispersed by the correct DM. This performs the correct compensation of the interstellar medium and hence re-aligns the pulses at all frequencies. The shaded blocks in both figures serve to highlight the shifting procedure.

Figure 3.4: Final array representing summation of all channels. Multiple time series are passed to the de-dispersion function, all are shifted in time by different amounts, and then summed. Thus only one time series is produced at the output.

	Time Sample Number					
	0	**1**	**2**	**3**	**4**	**...**
Channel Summation =	4	28	3	3	2	

Figure 3.4 shows the final output of the de-dispersion stage which is simply the summation of all the channels. Thus the input to the de-dispersion stage is a number of time series corresponding to the number of channels; and the output is one time series.

Integers have been used to illustrate the time sample amplitudes. Clearly this will be in binary format and a bit resolution must be selected. Lower resolutions lead to faster computational times, however, care must be taken in the case of using a low resolution time sample, as the summing operation may lead to an overflow in some channels. This problem was overcome in the algorithm by using a larger bit resolution per sample for the array containing the summation of all the channels.

3.3.3 Dispersion Measure Step Size

Dispersion measure step size is an important parameter of the algorithm as it determines the computational efficiency and sensitivity. A derivation of the dependence of the S/N ratio on DM_{error} is given in [1]. DM_{error} being the difference between the DM value used by the algorithm and the true physical value. An intuitive method of selecting the DM step size is to equate the delay for the DM step size between the lowest and highest frequency channels to the sampling interval [1]. This involves a simple re-arrangement of equation 2.12 to:

$$DM_{stepsize} = \frac{t_{sample}}{4.15 \times 10^6 \ ms} \times \left(f_{lowest}^{-2} - f_{highest}^{-2} \right)^{-1} \qquad \text{(Eq. 3.2)}$$

This gives a step size that moves the lowest frequency channel back in the time series by one sample value. The sample shift that the intermediate channels experience is rounded to the nearest integer.

3.3.4 Trial Dispersion Measure Range

As discussed in section 2.4.2 , electron density varies in the Galaxy. Computational time can be saved by taking the telescope beam co-ordinates into account when iterating through DM values. The function inputs are the equatorial co-ordinates which are retrieved from the header of the raw data file. These co-ordinates are transformed into Galactic co-ordinates to simplify the condition statements to follow. The minimum DM is set to zero as a default, however, this can be increased to reduce computation time. The maximum DM is given by a crude approximation of [13] for that particular set of coordinates. This maximum value is multiplied by a factor of 2 to compensate for uncertainties. This is suggested by [1].

3.3.5 Preparation for the multi radix FFT

The resulting array from the de-dispersion and channel summing process is now Fourier transformed. Using the Fastest Fourier Transform in the West (FFTW) C library, the Discrete Fourier Transform can be optimized if the number of time samples is a factor of the expression $2^a \times 3^b \times 5^c \times 7^d \times 11^e$ where *a, b, c, d, e* are whole numbers. This is referred to as a mixed radix FFT. The data is passed through a function that takes an array N samples long and finds the closest factor of $2^a \times 3^b \times 5^c \times 7^d \times 11^e$ that is less than N. The function divides N by prime numbers starting with 2 until the remainder is not equal to zero. It then moves to the next prime number and repeats the process. Once 11 is reached the resulting remainder R is stored. The sumChans array is then shortened by R values to make it a factor of $2^a \times 3^b \times 5^c \times 7^d \times 11^e$. Discarding data might be cause for concern however simulations showed that an insignificant number of samples (< 5 %) were discarded. Obviously a mathematical proof involving number theory is required here. A 4th year UCT student majoring in pure Maths was approached with the problem, however was unsuccessful in the allotted time. The fact that observation times can be chosen with this in mind also gives justification for discarding time sample. The time series has now been modified appropriately for an optimal Fast Fourier Transform algorithm to be applied.

3.3.6 Transforming to the Discrete Frequency Domain

The FFTW is subdivided into a number of functions that accept different types of input arrays. In the case of radio telescope time series data, the signals are real and hence a real to complex transform was used. This type of transform introduces a redundancy in that the Discrete Fourier Transform is symmetrical around the Nyquist frequency (i.e half the sampling frequency). This can be exploited by only computing the first (N-R)/2 Fourier components. Further computational efficiency can be achieved from noting the fact that pulsar periods generally only range between 1 millisecond and 10 seconds. Further reductions in computational time can be introduced if a particular period range is desired (e.g. millisecond pulsars).

A time series of sample length N and sample interval t_{samp} is transformed by the FFTW

real to complex function to return an array, F_k, of length N. Exploiting the symmetry of the transform, only the real and imaginary components of the first N/2 Fourier components are returned, as the latter N/2 components will be mirrored. The FFTW created array F_k has the first N/2 real components stored in F_k for $0 \le k \le$ N/2 -1 and the corresponding imaginary components stored in F_{N-k} with F_0 representing DC. The real and imaginary parts are squared and summed to to find the power spectrum
(i.e. Power Spectrum [k] = $(F_k)^2 + (F_{N-k})^2$). F_0 is just squared, as it does not have an imaginary component.

The frequency resolution is determined by the observation length. The change in frequency between two adjacent values is given by:

$$\Delta v \; = \; \frac{1}{N \; t_{samp}} \; = \; \frac{1}{observation \; time}$$ (Eq. 3.3)

hence the longer the integration time, the finer the frequency resolution. The frequency corresponding to a particular component is given by the formula:

$$v_k \; = \; \frac{k}{N \; t_{samp}} \; = \; \frac{k}{observation \; time}$$ (Eq. 3.4)

where $0 \le k \le$ N/2

3.3.7 Whitening noise and Calculating S/N ratios

These two procedures are described together as it is most efficient to perform them in the same function. White noise is defined as a flat curve in the frequency domain (i.e. level amplitude with no frequency dependence). However, due to Radio Frequency Interference (RFI), from the receiver and data acquisition systems, the lower end of the spectrum tends to have a higher noise level [2]. This is referred to as red noise in some texts. Red noise causes a non-linearity in the search for large amplitude Fourier components in the frequency domain, making threshold detection non-uniform. One approach to mitigating

the effect of red noise is to split the Fourier array into n segments where the integer n is user defined according to a sensitivity/computational efficiency decision. Each segment's median is calculated and subtracted from each sample in that particular segment. This results in a 'whitened' spectrum. The mean is not used as any large amplitude contributions within the segment would bias the value. The mean is also calculated in order to normalise the amplitudes by dividing each data point by the root mean square of the data set. This results in a spectrum with zero mean and unit root mean square. The Signal to Noise level of any spectral feature is now simply its amplitude. This is converted to decibels for plotting. [1]

3.3.8 Incoherent Harmonic Summing

The Fourier Transform of a sinusoidal function has no harmonics, only two large amplitude components at the function's positive and negative frequency. Because the pulsar signal has a duty cycle, it can be modelled as a periodic Rect function seen in Introductory Fourier Analysis courses. With particular reference to [5], the transform of this waveform produces a number of harmonics. The number of harmonics with amplitude comparable to that of the fundamental is given by the reciprocal of the duty cycle. So a typical pulsar with a pulse width that is 5% of the period will have 20 significant harmonics prevalent in the frequency domain. Clearly this is a significant amount of Fourier power that is 'lost' if only the fundamental frequency is considered. Thus a method devised by [9] is used to sum the fundamental with the 2nd, 4th, 8th, 16th and 32nd harmonics if desired. The approach is to sum each component in the original Power Spectrum with a harmonic multiple of that particular component.

To sum fundamental frequency of any prevalent spectral feature with its second harmonic: the kth component is added to the $2k^{th}$ component for the entire array. The resultant array is summed with the higher harmonics in a similar manner.

This increases the noise power by a factor $\sqrt{2}$, however for two frequency components of similar amplitude, an increase in signal power of 2. This results in a net gain of approximately $\sqrt{2}$ in S/N. Further harmonic summing results in a significant increase in

S/N, particularly for narrow width pulses. [1]

3.3.9 Threshold Detection and Saving Candidate Pulsar Information

The frequency domain is then searched for power components that exceed a threshold determined by the number of false alarms that are acceptable to the end user of the algorithm. The threshold level for real pulsar data is calculated by the equation 3.5

$$S/N_{threshold} = \frac{\sqrt{\ln(n_{samples})} - \sqrt{\pi/4}}{1 - \pi/4} \qquad (Eq.\ 3.5)$$

where: $n_{samples}$ is the number of samples of the spectrum

A derivation and motivation of this threshold is given in [1]. If a candidate is found, its S/N ratio, DM, period and equatorial co-ordinates are saved to a candidate file. Once this is complete the entire process is repeated with the original n time series channels, however with the next iteration of the DM set.

Thus the final output of the algorithm is a file of candidate pulsars, each with their respective DM, period, S/N and equatorial co-ordinates saved. The header of this file will provide all global variables used for that particular run of the algorithm.

3.4 Additional Functions in Future Work

3.4.1 Barycentering

The theory required for barycentric corrections was outlined in Chapter 2. The corrections were not implemented in this project due to a lack of time. For sensitive searches, barycentric corrections should most certainly be applied, particularly for integration times longer than 30 minutes, as outlined in [1]. Due to the process involving a shifting of time samples, it would seem sensible to integrate this function within the de-dispersion stage in order to enhance the computational efficiency.

3.4.2 Galactic Electron Density Model

The dispersion measure range function (Section 3.3.4) implements a crude analytical approximation of Figure 3.5 below. The plot is found in [13]

Figure 3.5: Maximum DM values predicted by NE2001 as a function of Galactic Longitude. The top curve is for Galactic latitudes within 5° of the Galactic plane. The bottom curve is for Galactic latitudes outside this range.
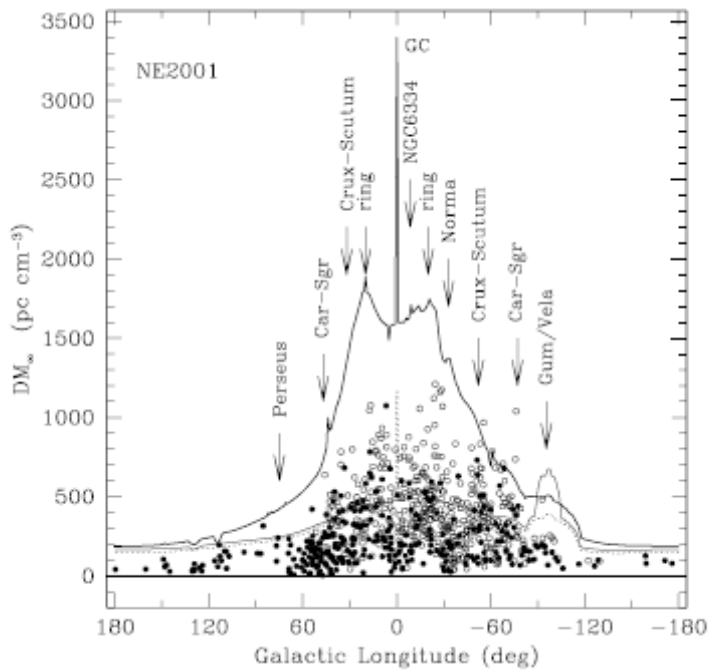
Function 3.3.4's crude approximation separates the Galaxy into 4 parts. Further computational efficiency can be achieved by reading in the complete set of data points mapped in [13] and thus achieving a higher resolution maximum DM data set. [6] and [13] explain the process, however both papers are relatively lengthy and time did not permit a full investigation into this.

Chapter 4

Testing

Chapter 4 reports the algorithm's performance in the processing of simulated pulsar data. The data is obtained from a package called SIGPROC written by Dr Duncan Lorimer, a pulsar astronomer. A number of different parameters can be simulated. The approach taken in this chapter is to test each function in the algorithm with one set of pulsar parameters. The path of the simulated pulsar data will be described through each relevant step in the algorithm and plotted for quantitative analysis.

4.1 Overview of Testing Procedure

The focus of the testing procedure was to demonstrate the functionality of the algorithm. A coherent plan on how to perform the testing is clearly needed, particularly considering the large number of parameters involved. A block digram of the testing procedure devised is given in Figure 4.1.

Figure 4.1: The block diagram shows how three sets of time series data are simulated –

Time series A with no dispersion or de-dispersion; B with dispersion but no de-dispersion; and C with both dispersion and de-dispersion. Each is Fourier Transformed and the respective spectra compared. Time series C's spectrum is then 'whitened' and normalised by the rms value of the spectrum. The resulting spectrum is searched for pulsar candidates and an example of the output file is given. For illustration, the spectrum is searched for candidates using a range of DM values. The resulting S/N ratios of any candidates found are plotted against the respective DM values.
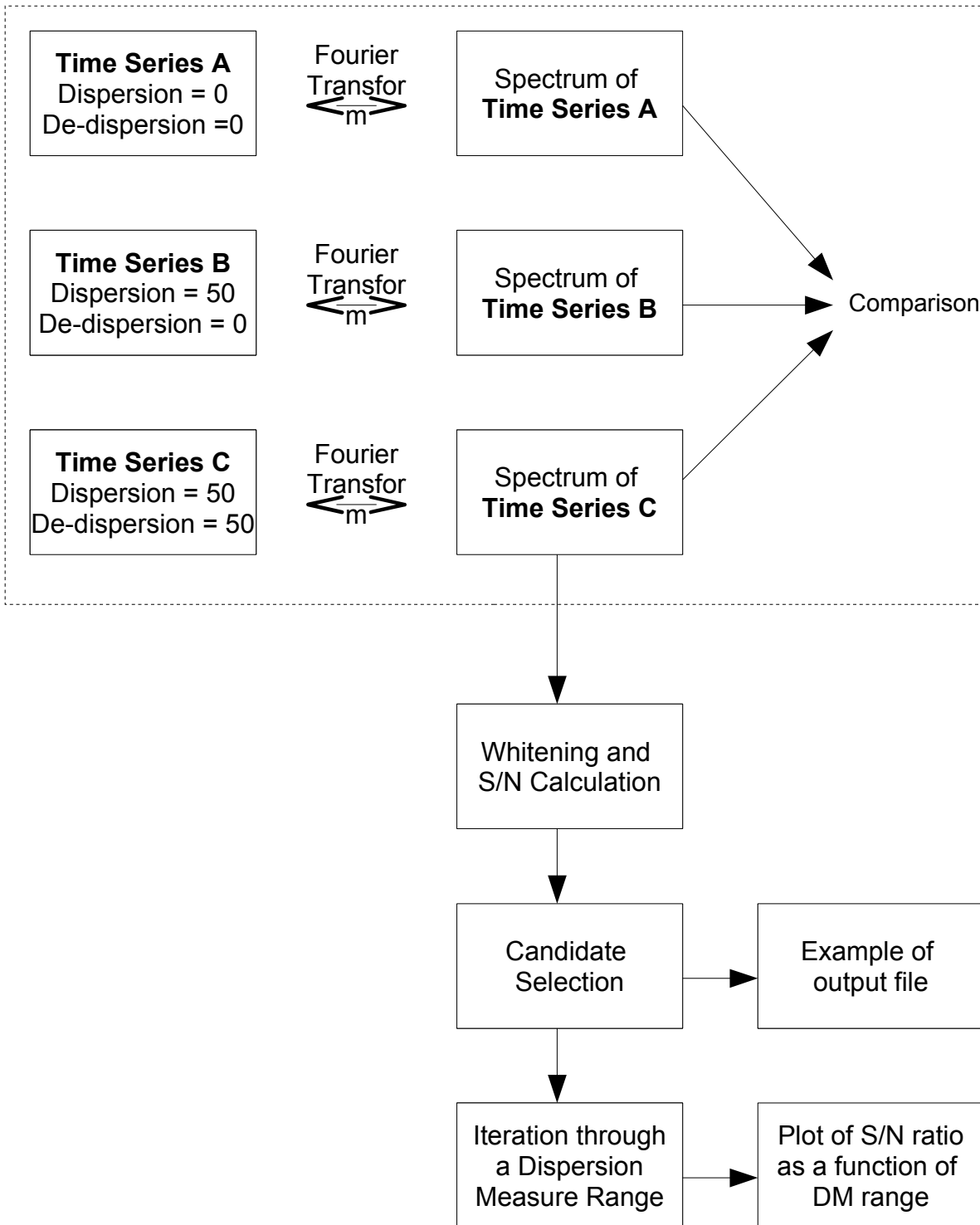
4.2 Simulation Parameters

The parameters used to generate simulated data and testing are listed in Table 4.1.

Table 4.1: Relevant pulsar data simulation parameters used in the test case reported in this document.

Parameter	Value
Period	104 ms
S/N peak	10 (arbitrary units)
Duty cycle	10.1%
Highest Frequency Channel	450.14 MHz
Number of channels	128
Sampling Interval	496 µs
Channel Bandwidth	1 MHz
Length of Observation	50 seconds
Number of bits per sample	8

A brief motivation for the choice of each value in Table 4.1 is given below. This is important because some values were constrained by hardware limitations.

4.2.1 Period

The value of 104 ms is chosen to be logarithmically centered on the known pulsar period range (approximately 1 ms to 10 s).

4.2.2 S/N peak

This is the ratio of the time series pulse peak to the rms of the Gaussian noise added. The relatively high value of 10 was chosen to enable the time series plots to clearly show the pulsar signal.

4.2.3 Duty Cycle

Pulsar duty cycles range between 1% and 50% with a typical value of 5% [1]. 10.1% was chosen so that fewer harmonics of significant amplitude, and hence clearer spectrum plots. It also enables a clearer graph of the time series.

4.2.4 Highest Frequency Channel

Most pulsar searches have taken used frequencies in the range 400 – 450 MHz.

4.2.5 Number of Channels

128 is relatively typical of previous pulsar searches.

4.2.6 Sampling Interval

The shortest known pulsar period is 1.6 ms. To resolve this the sampling interval should be at least half this value.

4.2.7 Channel Bandwidth

A 1 MHz channel bandwidth is clearly impractical, however was chosen to better illustrate the effects of dispersion and de-dispersion. In practice this value must be carefully selected as it involves a trade-off of recovered S/N ratio and computational efficiency. This is because the larger the channel bandwidth, the larger the portion of the spectrum that is moved erroneously resulting in a lower pulse amplitude when channels are summed.

4.2.8 Length of Observation

50 seconds is short integration time but was chosen to reduce memory demands. The short integration time was compensated by the high S/N peak specified.

4.2.9 Number of bits per sample

This is user defined. The algorithm allows values of 4, 8, 16, 32. 8 was chosen for sufficient amplitude resolution and computational efficiency.

4.3 Results of Testing Procedure

The respective stages outlined in the testing overview diagram (Diagram 4.1) are now plotted for illustration and discussed.

4.3.1 Reference Case

A set of time series of zero dispersion and zero de-dispersion generated as a reference for the performance of the algorithm. This set is passed to the de-dispersion function, however from equation 2.12 it can be seen that no shifting will take place. A portion of the resulting channel-summed time series is plotted in Figure 4.3.1 to illustrate the pulsar signal. The plot shows approximately 5 periods in 0.5 seconds, consistent with the 104 ms period. The high S/N peak is clearly seen.

Figure 4.2: Plot of summation of time series of all channels using parameters from Table 4.1. Approximately 5 periods can be seen in the first 0.5 seconds corresponding to a period of 104 ms. The S/N peak of the pulse amplitude is 10.
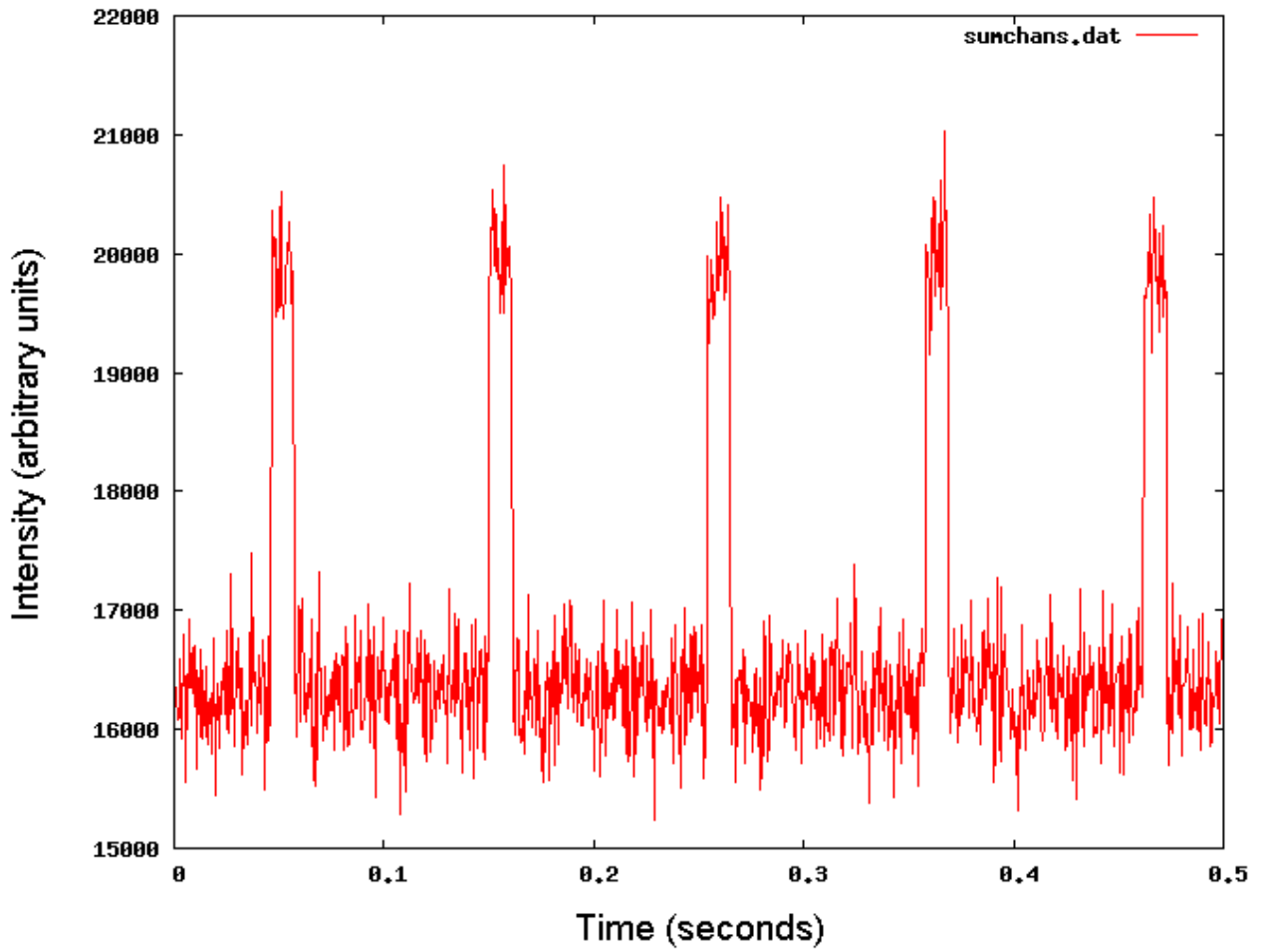
4.3.2 The Time Series Effect of Dispersion

Figure 4.3.2 shows the same time series the reference case in Figure 4.3.1, however the simulated data was dispersed by a DM = 50 pc.cm^{-3} . This DM value was chosen as it is typical maximum DM value for most parts of the sky (i.e. non-Galactic plane). The effect of dispersion smearing out the pulses is clearly seen. The maximum amplitude has dropped considerably right down to the noise level.

Figure 4.3: Plot of summation of time series of all channels where the data have been dispersed by a DM = 50 pc.cm^{-3}. The pulses have been smeared, burying them in the noise.
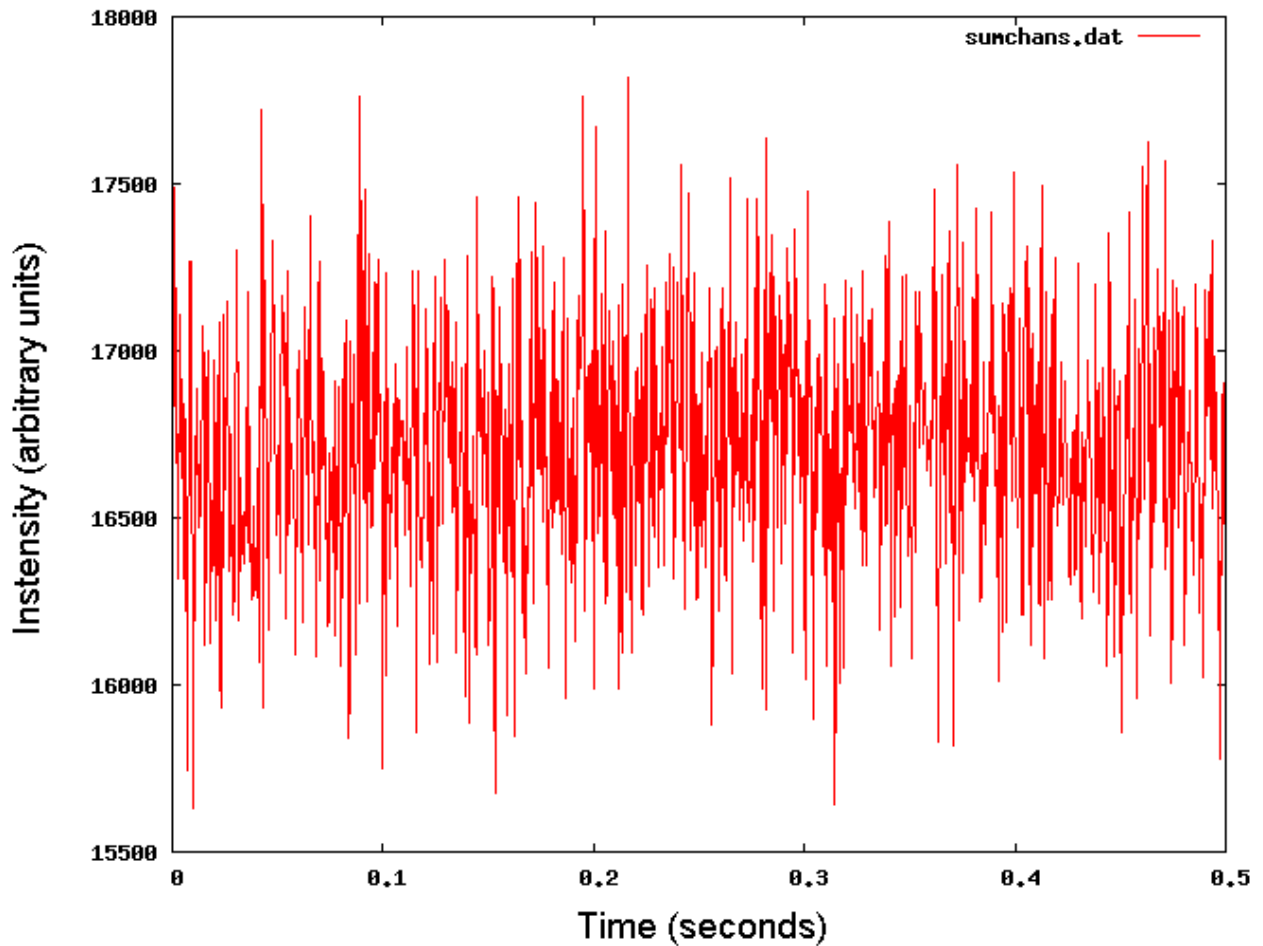
4.3.3 Effect of De-dispersion Function on a Dispersed Time Series

The same time series in 4.3.2 that has been dispersed by DM = 50 pc.cm^{-3} is now de-dispersed by the same DM value. The pulse structure is clearly recovered and the pulse peak level is approximately the same as in the zero dispersion, zero de-dispersion case in 4.3.1. Note again that the time series comparisons are done to give an illustration of the effects of dispersion and de-dispersion on the pulse profile. A more quantitative analysis is taken with the spectra of the three cases.

Figure 4.4: Plot of summation of times series of all channels where the the data have been dispersed and de-dispersed by a DM value of 50 pc.cm^{-3}. The pulses have been recovered from the noise and the S/N pulse peak of 10 is regained.
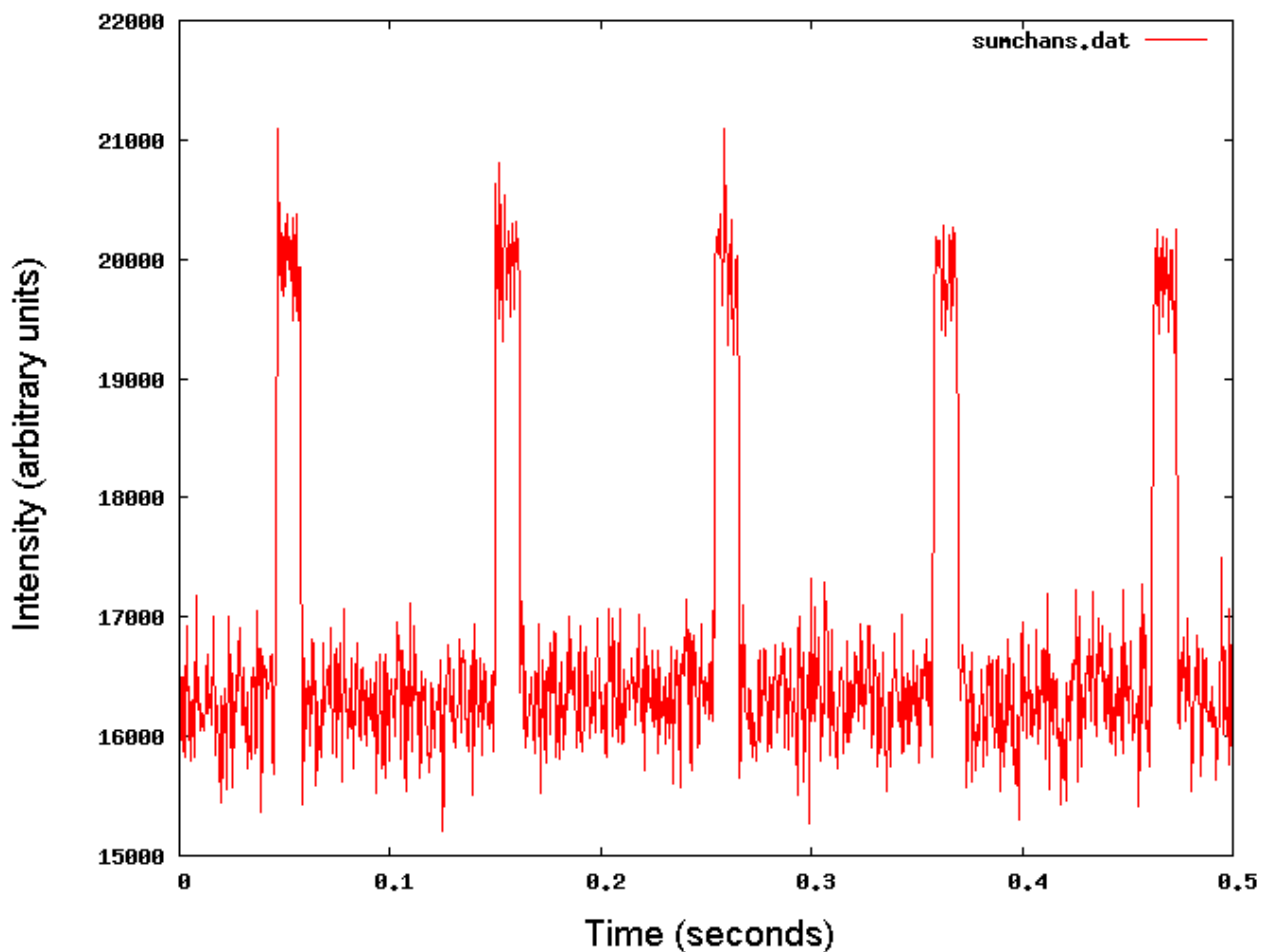
4.3.4 Spectrum of Sampled Periodic Pulse

The DFT of a train of pulses follows the envelope of a Sa^2 function [5]

where: $$Sa^2(x) \left(\frac{\sin x}{x} \right)^2$$

As discussed in Section 3.3.8 the number of harmonics with an amplitude comparable to the fundamental is inversely proportional to the duty cycle. There is a large DC component that has not been included in the plot to better illustrate the profile of the spectrum. This is done for all spectrum plots that follow in this document.

Figure 4.5: Plot of a selected range of the spectrum of the simulated periodic pulsar data. The parameters from Table 4.1 have been used as well as zero dispersion and zero de-dispersion. The plot serves to illustrate the profile of the Discrete Fourier Transform of a train of pulses. It follows the envelope of a Sa^2 function with the number of harmonics determined by the duty cycle of the pulsar. The large DC component has not been included in the plot for improved illustration.
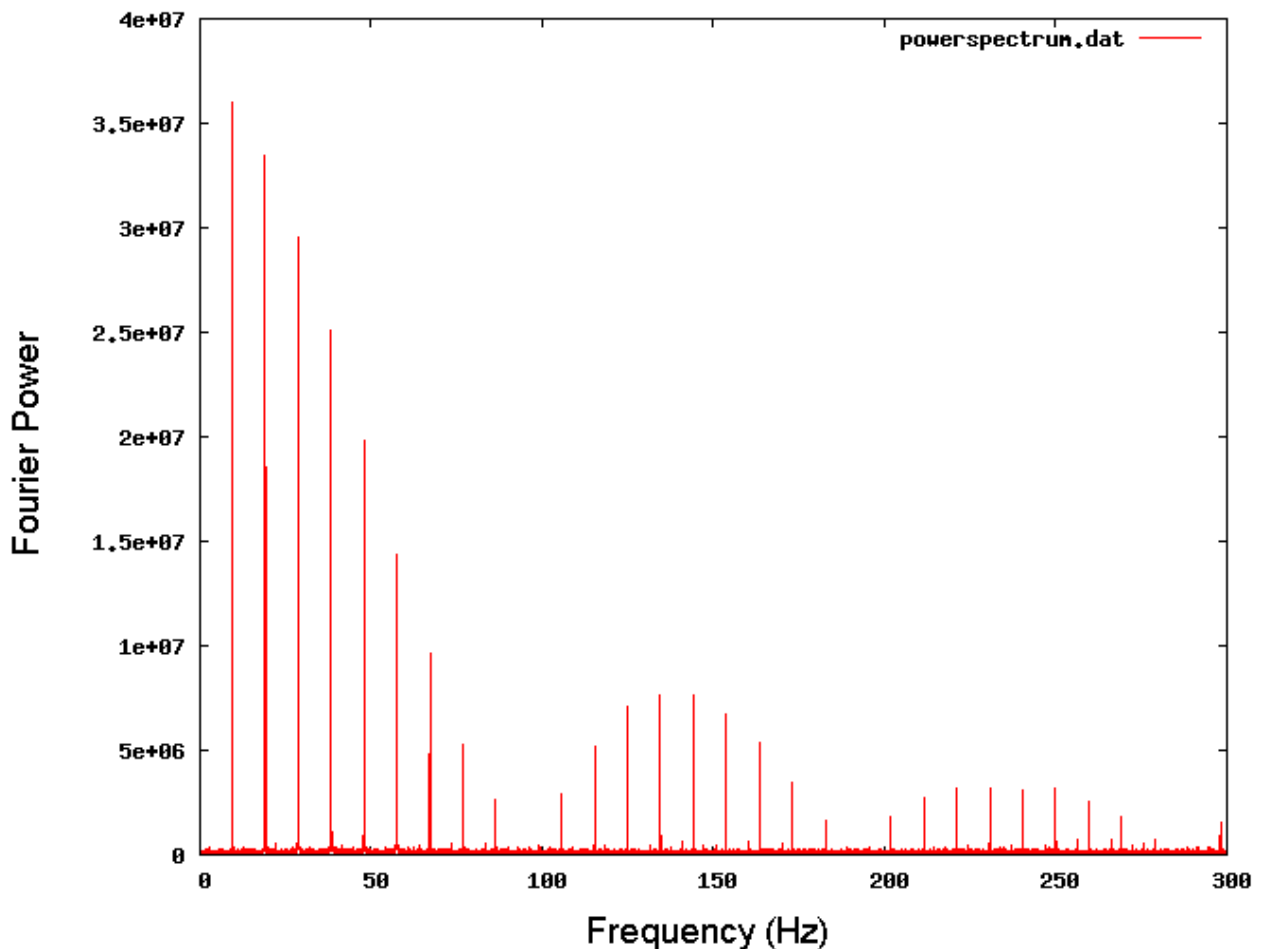
4.3.5 Spectrum of Reference Time Series

The reference time series described in 4.3.1 of zero dispersion is Fourier Transformed and its spectrum plotted in Figure 4.3.5. The fundamental frequency of approximately 10 Hz can be seen along with its harmonics. The amplitude of the fundamental will be used to quantitatively measure the effect of dispersion alone, followed by both dispersion and de-dispersion. The large DC component has not been plotted to enable the fundamental frequency and its harmonics to viewed in more detail.

Figure 4.6: Plot of spectrum of a time series that has had zero dispersion and zero de-dispersion. The plot has been zoomed in to only show the significant harmonics of the fundamental frequency. The amplitude of the fundamental frequency in this plot is used as a reference for comparison with other spectra.
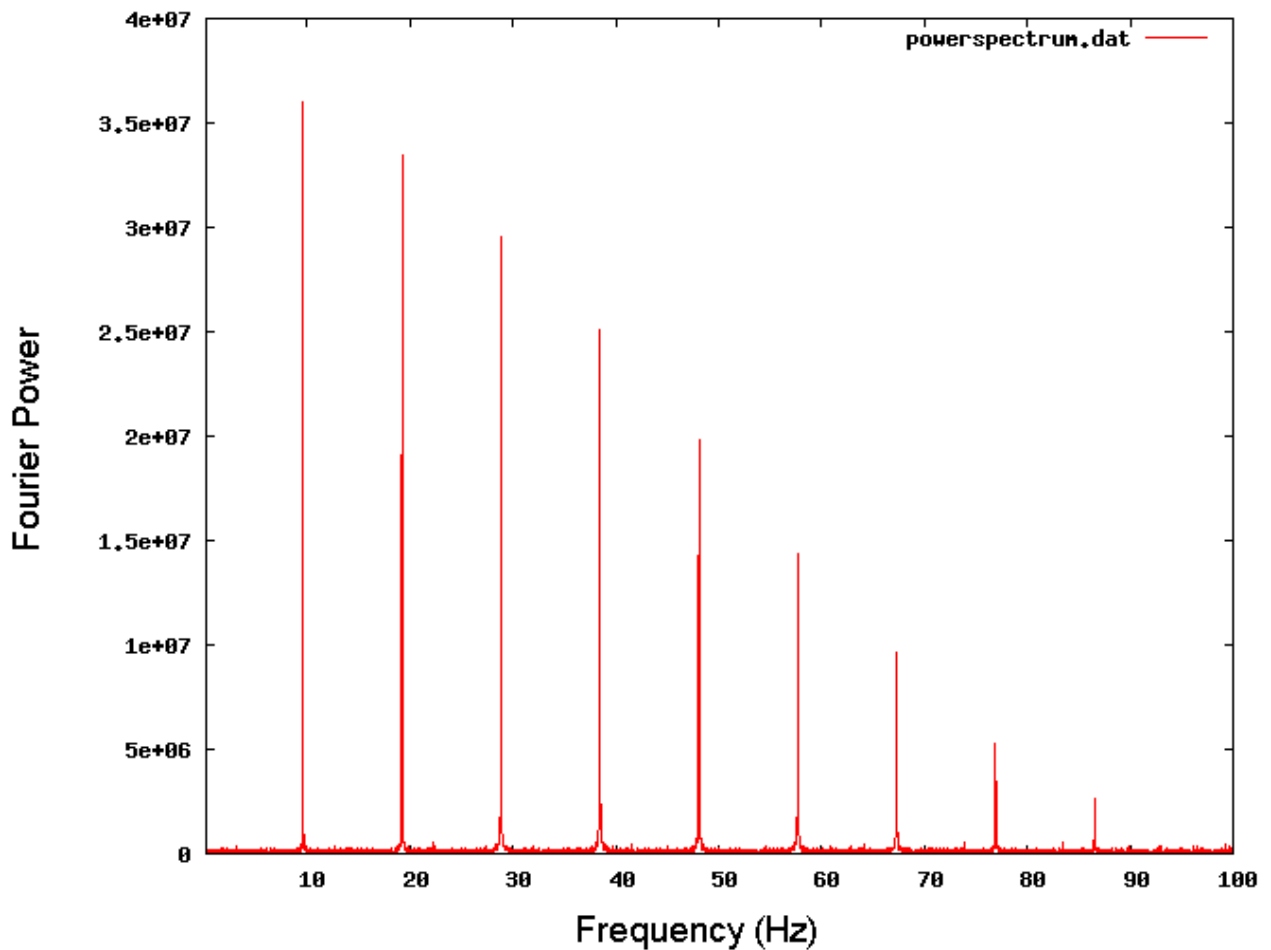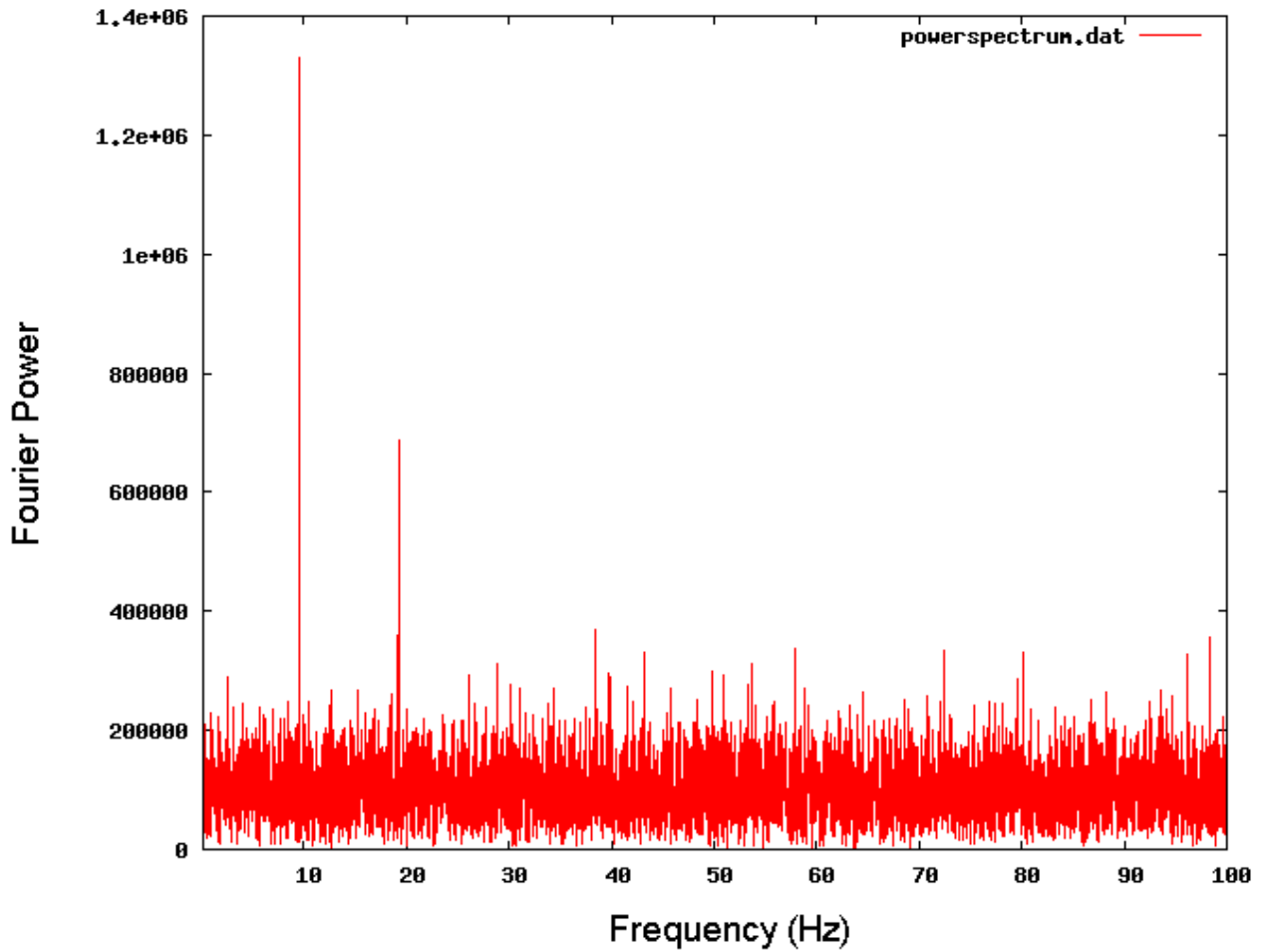
4.3.6 Spectrum of a Dispersed Time Series

The spectrum of the dispersed time series described in 4.3.2 shows the effects of the interstellar medium described in Chapter 2. Recall that the time series has been has been smeared in the time domain. This causes the two differences seen when comparing Figure 4.7 with the zero dispersion spectrum in Figure 4.6. Firstly, the fundamental frequency amplitude has decreased by a factor of 27. This corresponds to a drop in S/N of 14 dB. Secondly, the number of significant harmonics has decreased from 9 to 1. This is consistent with the smearing of the pulse in the time domain increasing its duty cycle and hence decreasing the number of significant harmonics.

It is worth taking a step back and noting that this is the spectrum that is obtained without applying the algorithm on pulsar radiation incident to Earth's orbit. This illustrates the weak nature of the unprocessed pulsar signal.

Figure 4.7: Plot of spectrum of a time series that has been dispersed by a DM value of 50 pc.cm^{-3} and zero de-dispersion. The amplitude of the fundamental frequency has decreased by 14 dB with respect to the plot in Figure 4.3.5. The number of significant harmonics has decreased to 1. This plot clearly shows the effects of dispersion in the frequency domain.

4.3.7 Spectrum of Recovered De-dispersed Time Series

Applying de-dispersion to pulsar data incident to a radio telescope will 'compress' pulses in the time domain and increase the power level of the spectral features in the frequency domain. This is seen in Figure 4.8, where the fundamental frequency's amplitude has increased by a factor of approximately 27 corresponding to an increase in S/N of 14 dB. The fundamental frequency amplitude is at approximately the same level as the fundamental frequency amplitude in the zero dispersion spectrum shown in Figure 4.6 The number of significant harmonics has increased to the number in the zero dispersion case.

Figure 4.8: Plot of spectrum of a time series that has been dispersed and de-dispersed by a DM value of 50 pc.cm^{-3}. The amplitude of the fundamental frequency has been recovered to approximately its original value seen in Figure 4.3.5. The number of significant harmonics has also been recovered. This plot shows the effectiveness of the de-dispersion function.
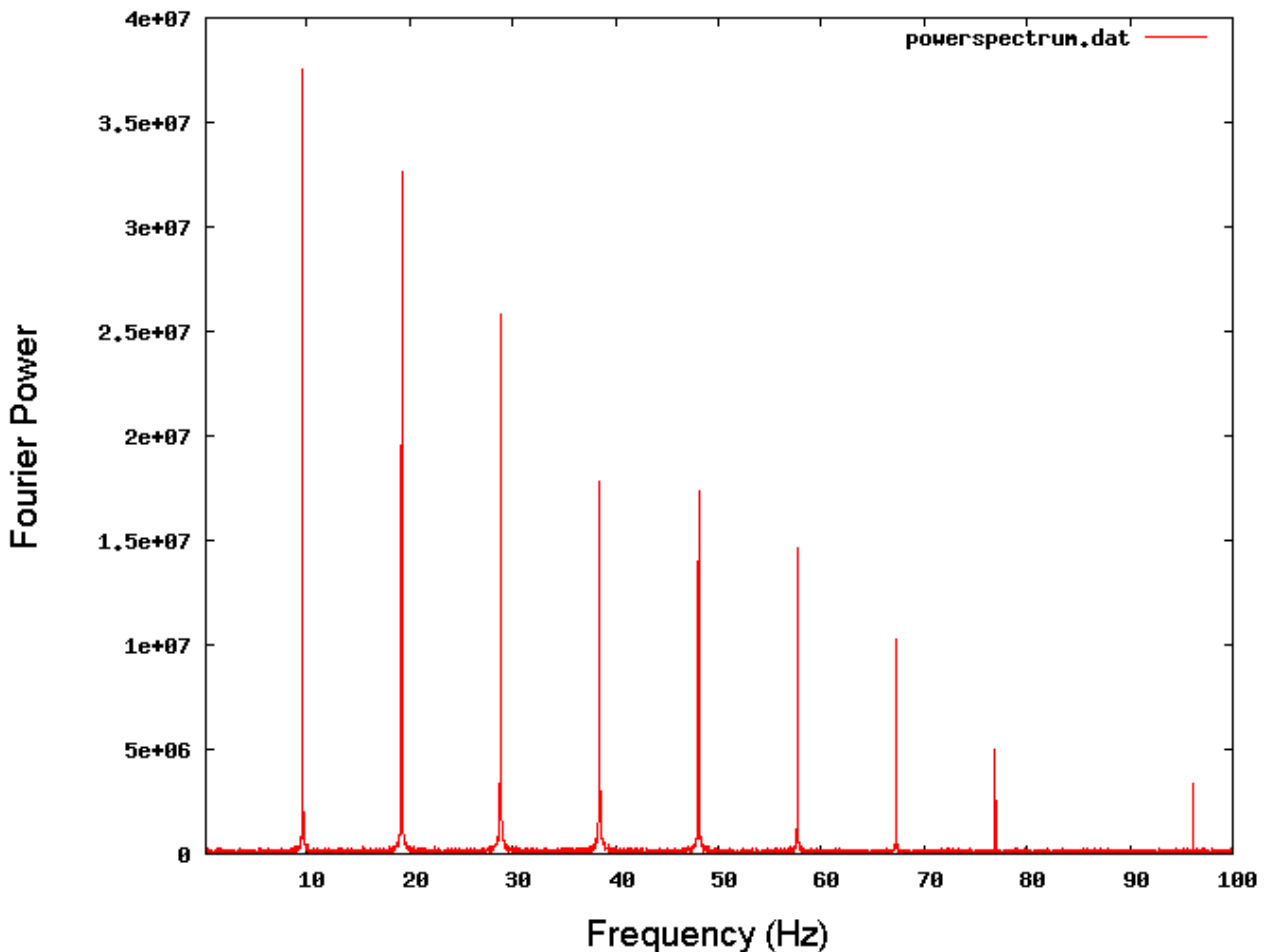
4.3.8 Whitened and Normalized Spectrum

Referring back to Figure 4.1 shows that the next step in the testing procedure is to demonstrate the performance of the 'Whitening and S/N Calculation' function. Recall that the two procedures are integrated into one function for computation efficiency reasons. The de-dispersed spectrum in Section 4.3.8 is whitened and normalized yielding the spectrum seen in Figure 4.9.

Figure 4.9: Plot of spectrum of dispersed/de-dispersed time series that has been normalized by the rms value of the spectrum. If this were real radio telescope data, the S/N ratio would be represented by the amplitude of a spectral feature. The spectrum has also been 'whitened', however the effect of this can not be seen as the simulated data does not include red noise.
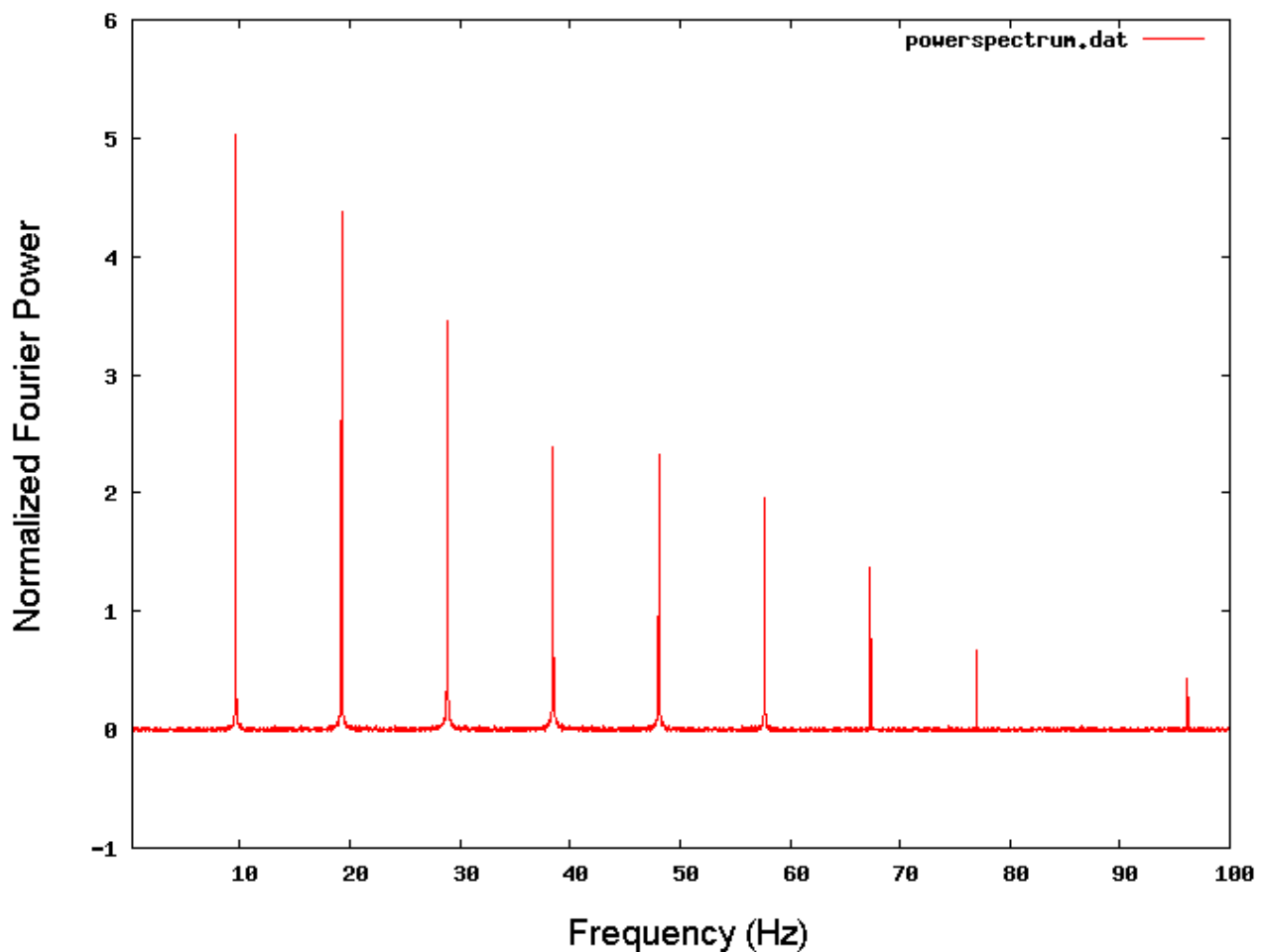
The pulsar data simulator does not simulate red noise, and so the whitening procedure is not illustrated in the above plot. For this reason, the spectrum of 100 ms periodic pulse with zero noise was added to simulated red noise. The rms of Gaussian noise was made inversely proportional to the frequency – grossly exaggerating, but effectively modelling red noise. In addition to this, the local mean value of the noise was also made inversely proportional to frequency. A plot of this simulated spectrum is shown in Figure 4.10 where the negative slope of the noise floor is clearly seen.

Figure 4.10: Spectrum of a 100 ms periodic signal with simulated pseudo red noise. The increasing rms and mean of the noise can be seen towards the lower end of the spectrum – thus modelling the effect that data acquisition systems have on the recorded data.

50
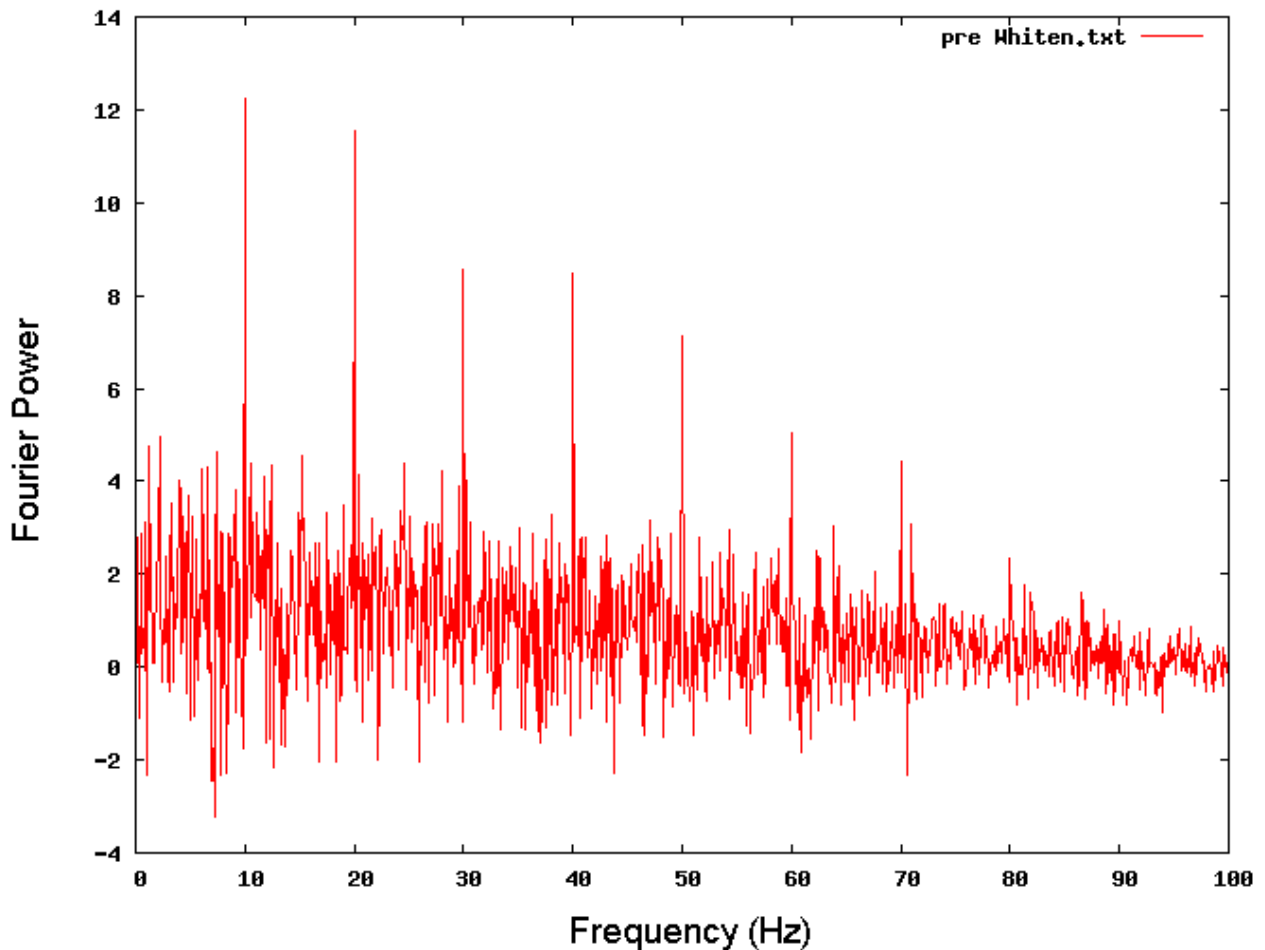
Applying the whitening and normalization function to this data set results in the noise floor to be centred on zero, the noise floor slope to be zeroed as well as amplitudes to represent S/N ratios (if the right scaling specific to the telescope parameters has been done in a frontend function). Figure 4.11 shows the data set in Figure 4.10 once it has been passed through the whitening and normalization function. The workings of this function are explained in section 3.3.7.

Figure 4.11: Spectrum of the pseudo red noise once it has been passed through the whitening function. The spectrum has been normalised by the local rms value. The fundamental frequency (10 Hz) is lower in amplitude than some of its harmonics. The reason for this is two-fold: statistical and the fact that it has been normalised by a higher rms value.
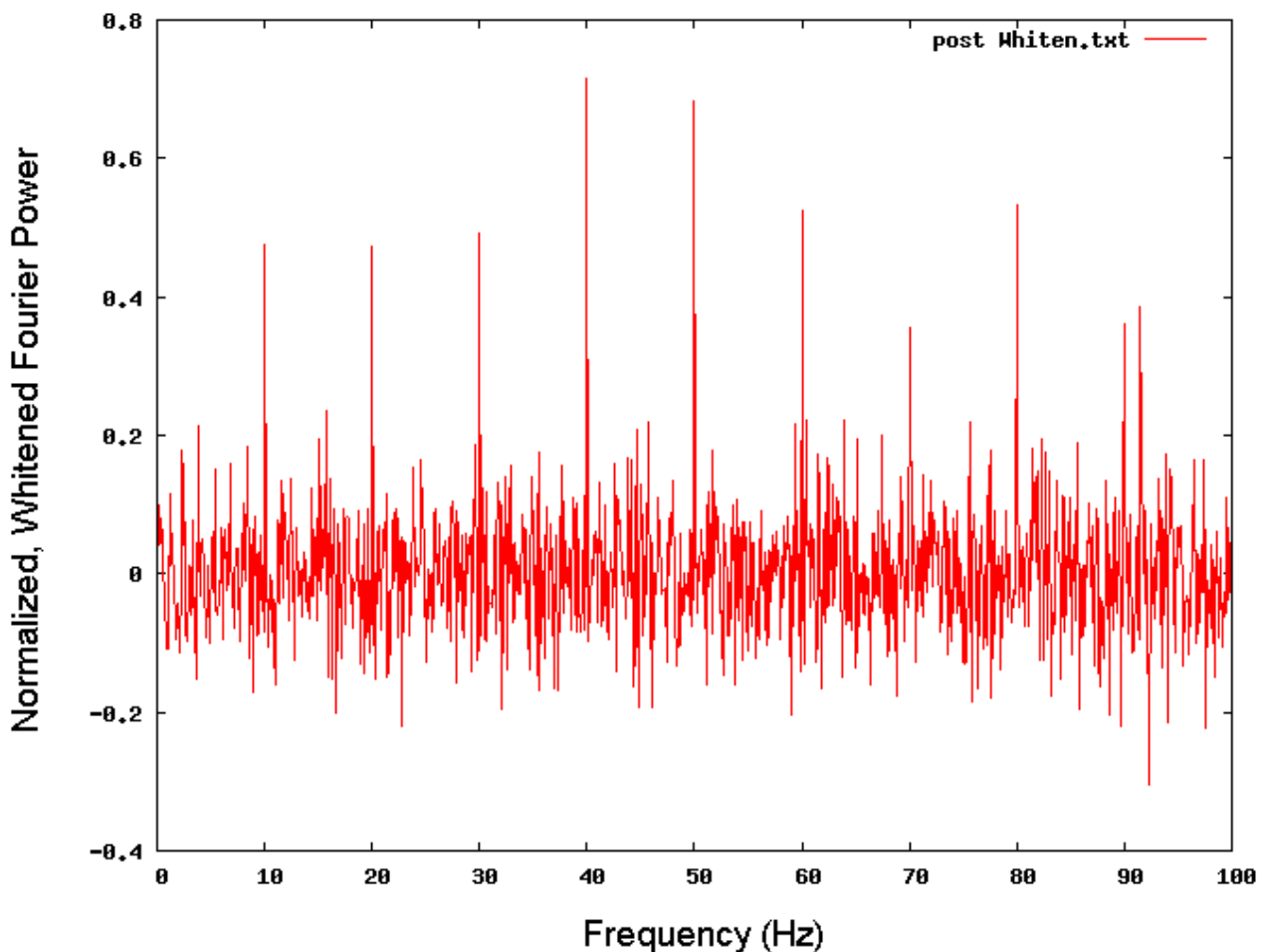
4.3.9 Incoherent Harmonic Summing

As described in Section 2.3.2 the number of significant harmonics is inversely proportional to the pulsar duty cycle. A substantial amount of power exists in the harmonics of a small duty cycle pulsar. Retrieving this power using the method described in Section 3.3.8 results in a increase in the S/N level of the fundamental frequency component. The normalized spectrum in 4.3.8 is passed into the Incoherent Harmonic Summing function yielding the spectrum in Figure 4.8. Two differences in this spectrum can be noticed immediately. Firstly, the amplitude of the fundamental frequency has increased by a factor of approximately 2.4. This corresponds to an increase of 3.4 dB. Performing harmonic summing adds considerably computational expense, however it is well justified with the increase in S/N level of the fundamental frequency. The S/N increase will become greater with decreasing pulsar duty cycles.

The second difference in of the input and output spectrum of the harmonic summing function is that a number of spurious spectral features appear. This is an artefact of the downsampling and summing of the original spectrum to achieve the harmonic summing. It is not of concern as the spurious components will always have a considerably lower amplitude than the fundamental frequency.

Figure 4.12: Plot of resultant spectrum once it has been passed through the Harmonic Summing function. The S/N ratio of the fundamental frequency has increased by 3.4 dB with respect to the input spectrum shown in Figure 4.7. Artefacts of the harmonic summing process can be seen in the form of spurious components. Since these are significantly lower in amplitude than the fundamental, they can be disregarded without concern.
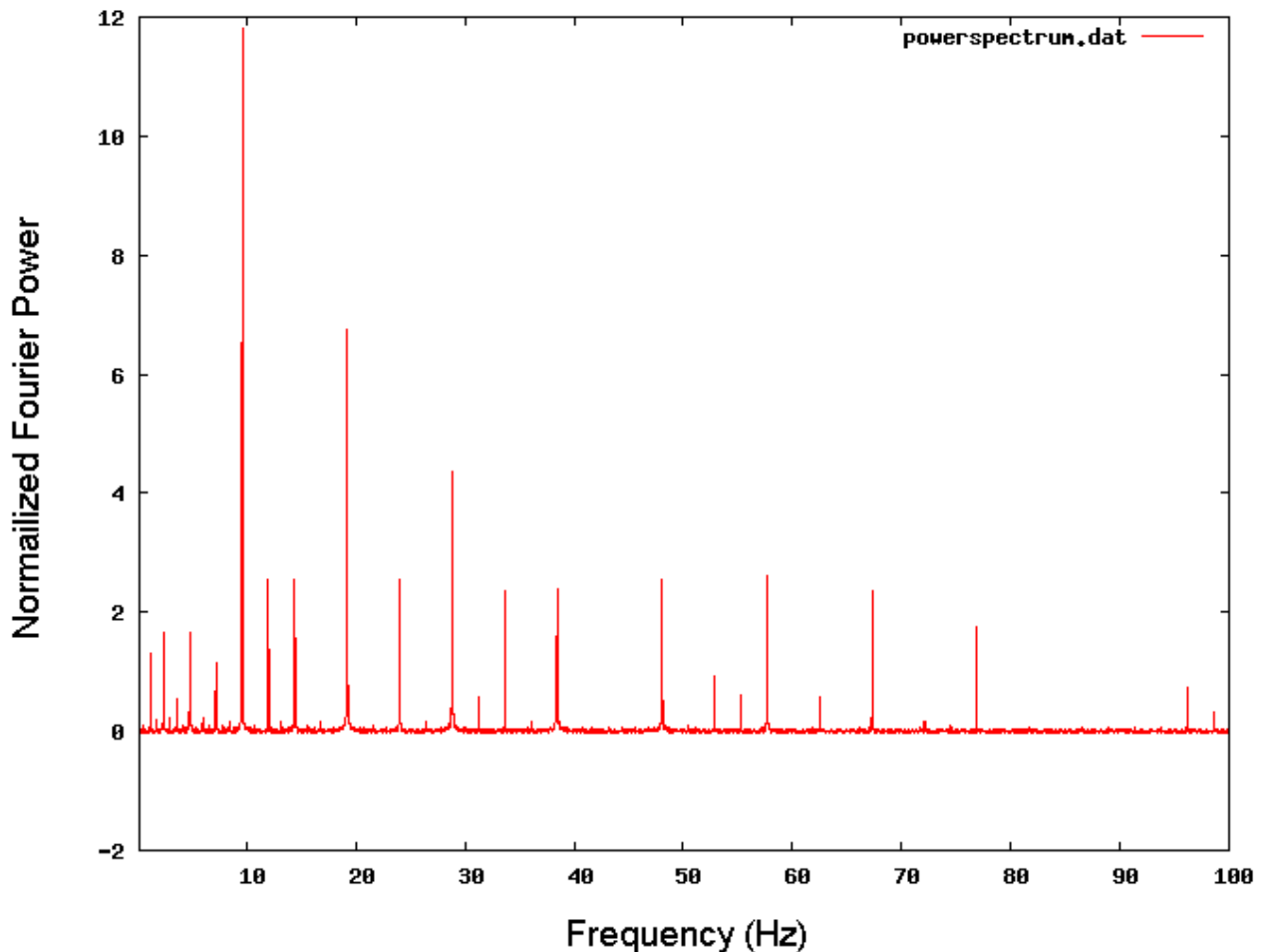
4.3.10 Pulsar Candidate Selection

The end point of the algorithm is a function that searches through the spectrum and returns any candidate pulsar. The threshold detection level for real data (where the radio telescope parameters are known) is discussed in Section 3.3.9. This is not feasible for the simulated data. Thus, a simple method of selecting the maximum amplitude in a spectrum was used to output a candidate pulsar to a log file. The header of this file contains all relevant parameters used in the algorithm. The DM, S/N ratio and Period of the candidate

pulsar are recorded. Figure 4.13 shows a screenshot of the log file for one trial DM value. This file is the final product of the algorithm and is what a pulsar astronomer would inspect to check the validity of candidates. The file generated in testing records a candidate for each spectrum searched. Clearly this is impractical and in the real case would not occur as a spectrum candidate would not be recorded unless it is above the threshold given by equation 3.5.

Figure 4.13: Screenshot of output file displaying pulsar candidates. The file displays all relevant parameters used in processing as well as the original pulsar parameters specified in the pulsar data simulator. The DM, S/N and Period of any candidates are recorded.

4.3.11 Iterating through a Dispersion Measure Range

In practice, the DM value of possible pulsars is unknown. Thus the algorithm is repeated as it iterates through a DM range. The DM step size described in Section 3.3.3 is relatively small (approximately 0.025 pc.cm^{-3} in this test case) requiring approximately 150 repetitions of the algorithm for the range 48 – 50 pc.cm^{-3} which took approximately 20 minutes to perform using a 1.8 GHz processor. Thus, a sense of the computational expense that pulsar searches demand is gained. The maximum S/N of the spectrum for the DM range was written to the log file described in Section 4.3.9. The recorded S/N ratios are then plotted against their respective DM values. As discussed in section 3.3.3, de-dispersing pulsar data with an incorrect DM value results in a reduced S/N ratio with respect to the correct DM value case. The mathematical relationship of this is derived in Appendix A. Clearly it is expected that as the algorithm iterates through the DM range, the S/N of the fundamental frequency would increase and reach a maximum as the trial DM value reaches the correct value. The S/N would then decrease as the trial value gets larger than the correct value. This is illustrated in Figure 4.14 with the S/N ratio peaking at DM = 50 pc.cm^{-3}. The trend shown in this plot is one of the tools pulsar astronomers use to verify a pulsar candidate to be authentic [1].

Figure 4.14: Plot of S/N ratio of fundamental frequency as a function of DM. The plot shows a clear peak at the true DM value of 50 pc.cm^{-3} specified in the simulated data. This type of plot provides strong evidence to the pulsar astronomer that the signal's origin is indeed a pulsar.
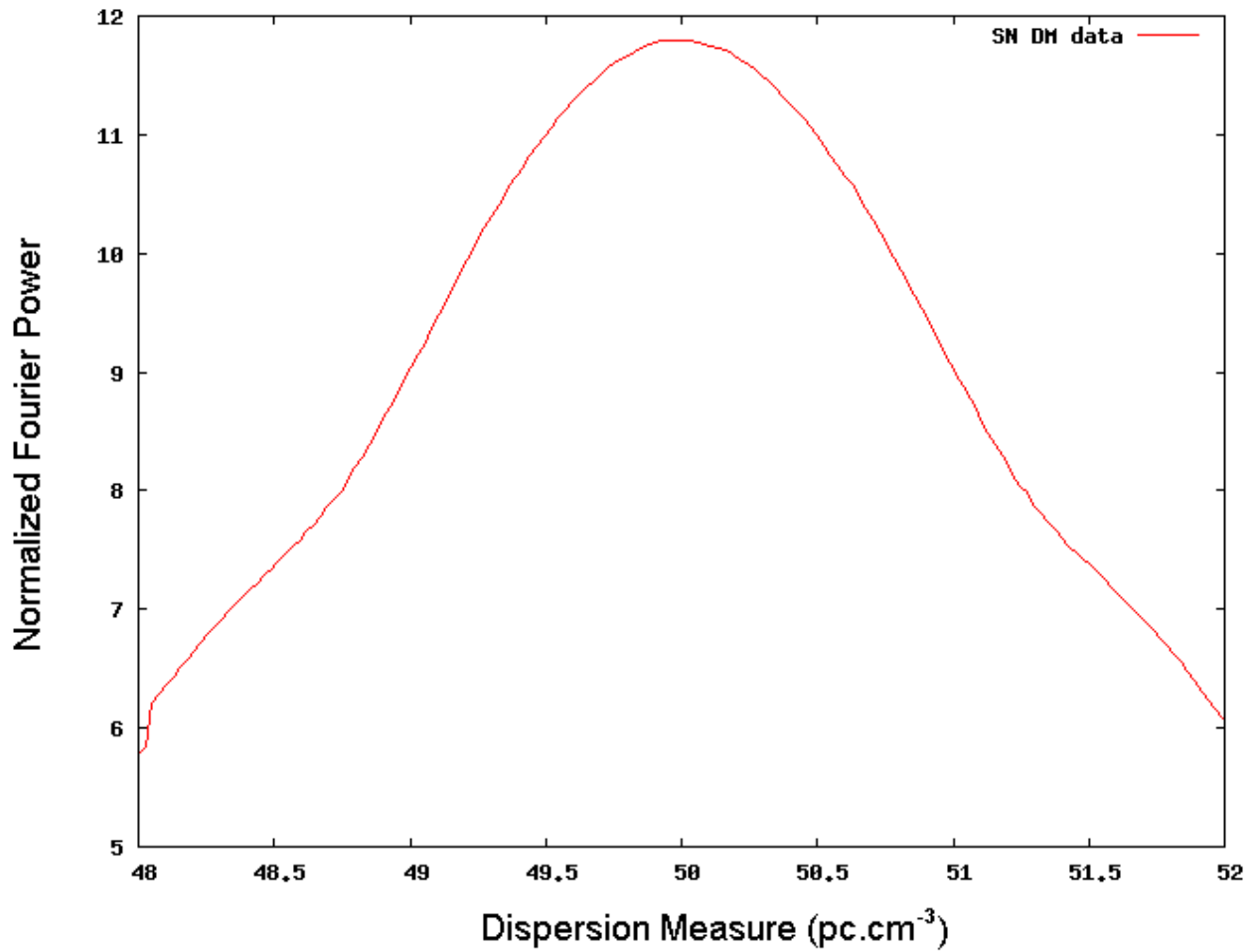
Chapter 5

Conclusions and Future Work

5.1 Conclusions

A theoretical background was built around the characteristics of pulsars and the radiation they emit with specific reference to their detection. A Pulsar Search Algorithm was coded that corrects for the effects of dispersion in the interstellar medium. A number of functions were included in the algorithm to improve the S/N ratio of the inherently weak pulsar signal. The algorithm has been designed with an ability to be modified to any radio telescope parameters as well as different types of searches. This satisfies the primary objective of the project.

The secondary objective of optimising the computational efficiency of the algorithm was partly fulfilled. Speed improvements were achieved through: on-the-fly de-dispersion and summing in the De-dispersion function; reducing the time series data to a relatively prime number to enable use of a multi radix FFT; and combining the whitening and S/N ratio normalization functions to be performed simultaneously. However, a number of possible improvements in speed were not investigated to keep the algorithm as simple as possible.

5.2 Future Work

With the basic framework in place for a simple pulsar search algorithm, a number of additional modules can be added to extend the algorithm's scope.

As discussed in Section 3.4 two aspects that should be furthered investigated and implemented are barycentering and more accurate use of the Galactic Electron Density Model. Barycentering enables the long integrations needed for weak sources to be carried out without losing S/N due to de-linearisation of the periodic pulse. Increased resolution in modelling the electron content in the Galaxy will improve the computational efficiency.

An additional module can be written to search for binary pulsars. This involves what is called an acceleration search. It requires a 3-D plot of pulsar spectra. The third dimension is the same spectra taken at different times. An orbiting pulsar will produce a vertical sinusoidal function in the S/N - Time plane.

Pulsar searches do seem to have been investigated thoroughly with little room for improvement on what has developed. Particular reference is given to the SIGPROC package written primarily by Dr Duncan Lorimer. It is recommended that this code be implemented as opposed to developing a new algorithm. Particularly in light of the extensive time spent on debugging code during the project.

It is recommended that the basic functions of the algorithm be simulated in a higher level language to grasp the concepts without too much effort spent on debugging.

Finally, with a view of the evolution of radio telescopes from large single dishes to large numbers of smaller dishes making up interferometers, it is tentatively suggested that new pulsar search techniques be investigated with raw interferometric data. An interferometer outputs what is referred to as the Visibility Function which is the Fourier Transform of the Source Brightness function which is simply the intensity measured in the interferometer's beam. It seems redundant to inverse Fourier Transform the Visibility function, apply de-dispersion and Fourier Transform back into the frequency domain. A method to search for pulsars directly in the Visibility Function could be investigated. No reference to this was

found in any of the source listed in References. This could be for good reason, but it was thought relevant to include it in future work.

_____

References

[1]   Lorimer D. R. & Kramer M., *Handbook of Pulsar Astronomy*, Cambridge University Press, United Kingdom, 2005

[2]   Lyne A. G.& Graham-Smith F., *Pulsar Astronomy*, 2nd Edition, Cambridge University Press, United Kingdom, 1998

[3]   Bignami, G. F., Caraveo, A., Luca, A. D., Mereghetti, S. 2003, *Neutron Star Magnetic Fields*, Nature, 423, 725

[4]   Carrol B.W., Ostlie D. A., *An Introduction to Modern Astrophysics*, International Edition, Addison-Wesley Publishing Company, Massachusetts, 1996

[5]   Morrison N, *Introduction to Fourier Analysis*, JohnWiley and Sons, New York, 1994

[6]   Cordes, J. M., Lazio, T. J. M., *NE2001. A New Model for the Galactic Distribution of Free Electrons and its Fluctuations*, 2002a, astro-ph/0207156 ,

[7]   Ables, J. G., Manchester, R. N., *Galactic Electron Densities*, 1976, A&A, 50, 177

[8]   Longair M. S., High Energy Astrophysics*,* 2nd Edition, Cambridge University Press, United Kingdom, 1994

[9]   Harmonic Series, http://mathworld.wolfram.com/HarmonicSeries.html, (accessed on 17 September 2006)

[10]   Pulsar Public Domain Catalogue, http://www.atnf.csiro.au/research/pulsar/psrcat, 2005

[11]   A Tutorial on Radio Pulsars, part of a M.Sc course taught at Jodrell Bank, 1996, http://www.atnf.csiro.au/research/pulsar/Tutorial/tut/tut.html

(accessed 15 September 2006)

[12] http://www.mpifr-bonn.mpg.de/pulsar/data/ (accessed 1st October 2006)

[13] Cordes, J. M., Lazio, T. J. M., *NE2001. A New Model for the Galactic Distribution of Free Electrons and its Fluctuations*, 2002b, astro-ph/0301598

[14] Chinese website, could not read text but copied image.
www.bamboo.hc.educ.tw (accessed on 21 September 2006)

[15] http://www.mpifr-bonn.mpg.de/div/pulsar/data/browser.html

[16] Chapter 3, AST3003S: Galactic and Extra-Galactic Astrophysics Lecture Slides
http://mensa.ast.uct.ac.za/~kraan/AST3003

Appendix A: Source Code

The source code for the entire project is provided on the attached CD. The README file in the root directory of the CD gives details of the layout of files.

Appendix B: Derivations

A1)   Dispersion Time Delay

$$v_g = c\,\mu$$

where the refractive index (μ) of the ISM is less than unity.

Thus the delay experienced by a radio signal travelling between the pulsar and Earth with respect to the speed of light is:

$$t = {}_0\!\int^d \frac{1}{v_g}.dl - \frac{d}{c}$$

Substituting v_g = cμ and making the observation that f_p << f to approximate μ, the expression for the time delay becomes:

$$t = \frac{1}{c} {}_0\!\int^d \left(1 - \left(\frac{f_p}{f}\right)^2\right)^{-\frac{1}{2}}.dl - \frac{d}{c}$$

substituting the expression for f_p yields:

$$t = \frac{e^2}{2\pi.m_e c} {}_0\!\int^d n_e.dl\left(\frac{1}{f^2}\right)$$

$$= \frac{D_{const} \times DM}{f^2}$$

A2) DM Step Size

Delay between two frequencies given by equation 2.12.

$$\Delta t \approx 4.15 \times 10^6 \, ms \times \left(f_1^{-2} - f_2^{-2} \right) \times DM$$

Setting delay to sampling interval yields:

$$t_{sample} \approx 4.15 \times 10^6 \, ms \times \left(f_1^{-2} - f_2^{-2} \right) \times DM_{stepsize}$$

rearranging and substituting the highest and lowest frequencies:

$$DM_{stepsize} \approx \frac{t_{sample}}{4.15 \times 10^6 \, ms} \times \left(f_{lowest}^{-2} - f_{highest}^{-2} \right)^{-1}$$

where the values of t_{sample} and $f_{highest}$ are retrieved directly from the data file header. f_{lowest} is calculated from:

$$f_{lowest} = f_{highest} - \text{number of channels} \times \text{channel bandwidth}$$